frontiers | Frontiers in Earth Science

TYPE Original Research
PUBLISHED 17 February 2023
DOI 10.3389/feart.2023.1109206

OPEN ACCESS

EDITED BY
Xiao-Ping Xia,
Guangzhou Institute of Geochemistry (CAS), China

REVIEWED BY
Ming Chen,
China University of Geosciences Wuhan, China
Yunying Zhang,
South China Sea Institute of Oceanology (CAS), China

*CORRESPONDENCE
Wenpeng Yang,
orcidme@163.com
Chenglu Li,
lcl230881@163.com

SPECIALTY SECTION
This article was submitted to Geochemistry, a section of the journal Frontiers in Earth Science

RECEIVED 27 November 2022
ACCEPTED 23 January 2023
PUBLISHED 17 February 2023

CITATION
Yang W, Li C, Alam M, Fu A, Zheng B, Yang Y and Hu X (2023), Geochemistry and geochronology of basic igneous rocks in Bairin Right banner, southeastern inner Mongolia, China: Implications for the final closure of the Paleo—Asian Ocean along the Xar Moron suture zone.
Front. Earth Sci. 11:1109206.
doi: 10.3389/feart.2023.1109206

Geochemistry and geochronology of basic igneous rocks in Bairin Right banner, southeastern inner Mongolia, China: Implications for the final closure of the Paleo—Asian Ocean along the Xar Moron suture zone

Wenpeng Yang[1]*, Chenglu Li[1,2]*, Masroor Alam[3], Anzong Fu[1], Bo Zheng[1], Yuanjiang Yang[1] and Xiaofang Hu[4]

[1]Natural Resources Survey Institute of Heilongjiang Province, Harbin, China, [2]Heilong Jiang Key Laboratory of Black Soil and Water Resources Research, Harbin, China, [3]Department of Earth Sciences, Karakoram International University, Gilgit, Pakistan, [4]Heilongjiang Geophysical and Geophysical Exploration Institute, Harbin, China

This paper reports the first discovery of basic igneous rocks in Bairin Right Banner in southeastern Inner Mongolia, China. To understand the genesis and tectonic evolution of these rocks, we have carried out geochronology and geochemistry research on them. The results show that LA-ICP-MS zircon U-Pb concordant mean ages of massive basalt, diabase, and pillow basalt are 272.0 ± 2.8 Ma, 261.5 ± 3.2 Ma, and 256.5 ± 2.5 Ma, respectively, suggesting their formation during the Late Permian. The massive basalt, diabase, and pillow basalt are tholeiitic with low $Mg^{\#}$ values in the ranges of 46.2–66.8, 54.4–71.0, and 53.5–58.2, respectively. They have similar chondrite-normalized rare earth element (REE) patterns. The intensity of REE differentiation is similar to that of typical enriched mid-ocean ridge basalts (E-MORB). The pillow basalts are relatively enriched in Ba and U, while slightly depleted in Rb and Th, and show geochemical affinity to E-MORB. The massive basalts and diabases have the same primitive mantle-normalized patterns and are relatively enriched in Rb, Ba, and U, while depleted in Nb and Ta, similar to the typical island arc magmas. Our new findings indicate that the intra-oceanic subduction of the Paleo-Asian Oceanic slab was still ongoing during the late Permian in the Bairin Right Banner area and, combined with previous studies, it might have been closed during the Late Permian to Early Triassic along the Xar Moron suture zone.

KEYWORDS

southeastern inner Mongolia, late permian to early triassic, basic igneous rocks, Xar Moron suture zone, Paleo-Asian Ocean

1 Introduction

The Central Asian Orogenic Belt (CAOB), located between the Siberian Craton and the Tarim-North China Craton (Figure 1A), is one of the largest accretionary orogenic belts of the Phanerozoic. It is an important window and natural laboratory for studying the process of crustal accretion and the mechanism of continental growth. In the CAOB, different scientists have discussed the formation of island arcs and accretionary complexes (e.g.,

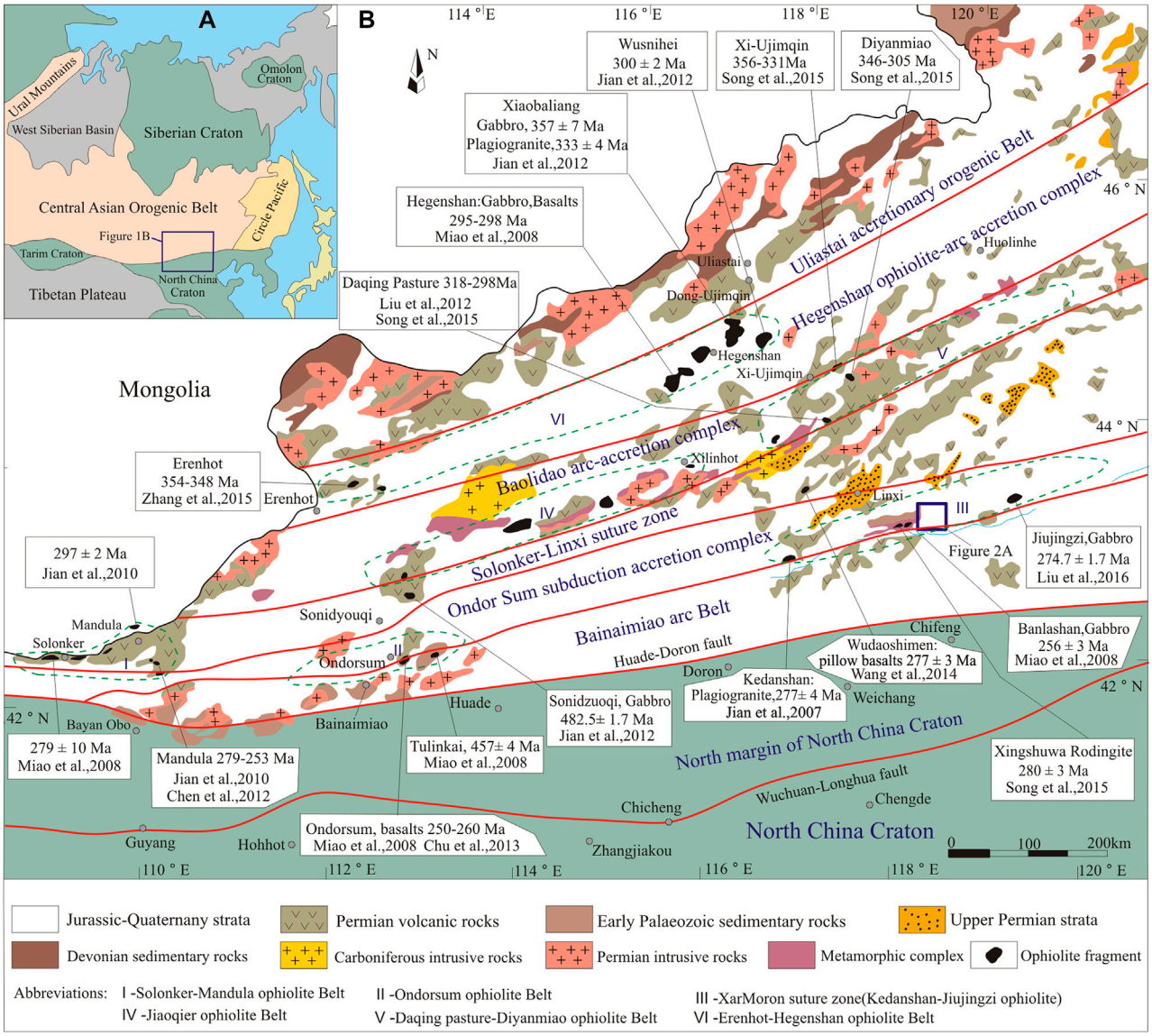

FIGURE 1
(A) Schematic diagram showing the main tectonic subdivisions of Central and Eastern Asia (Song et al., 2015). **(B)** Geological map of central Inner Mongolia of the CAOB showing tectonic units (Xiao et al., 2003; Song et al., 2015; Li et al., 2019).

Sengör et al., 1993; Windley et al., 2007; Zhou et al., 2009; Yang et al., 2019), geochronology and geochemistry (e.g., Li et al., 2011; Wu et al., 2011; Eizenhöfer et al., 2014; Tong et al., 2015; Shi et al., 2016; Zhao et al., 2020; Tang et al., 2021), regional tectonic frameworks (e.g., Chu et al., 2013; Xu et al., 2015; Tian et al., 2018; Pang et al., 2020), and ophiolites (e.g., Zhou et al., 2015; Luo et al., 2016; Xu et al., 2019). Inner Mongolia, which is located in the southeast of the Central Asian Orogenic Belt, has a complex tectonic evolution history, including a series of tectono-magmatic activities such as subduction, collisional orogeny, and post-orogenic extension of the Paleo-Asian Ocean. Tectonic units can be divided into the Bainaimiao arc belt, Ondor Sum subduction accretion complex, Solonker-Linxi suture zone, Baolidao arc-accretion complex, Hegenshan ophiolite-arc-accretion complex, and Uliastai accretionary orogenic belt, respectively (Figure 1B; Miao et al., 2008; Xiao et al., 2009; Jian et al., 2012; Xu et al., 2013, 2015; Song et al., 2015). The timing of the final closure of the Paleo-Asian Ocean and the subsequent collision between the Siberian and the North China plates along with the location of the collision are still debated. On the one hand, the closure of the Paleo-Asian Ocean is controversially thought to have happened during the following periods: pre-middle Devonian (Xu et al., 2014; Xu et al., 2015), Devonian or Early Carboniferous (Sengör et al., 1993; Robinson et al., 1999), or Late Permian to Early Triassic (Wang and Fan, 1997; Xiao et al., 2003; Li, 2006; Li et al., 2007; Miao et al., 2008; Xiao et al., 2009; Jian et al., 2010; Wu et al., 2011; Liu et al., 2016; Li et al., 2019). On the other hand, the final suturing location of the two plates is argued to have been found in the following locations: Gaijiadian-Balengshan in the Northwest of Solonker-Linxi (Xiao et al., 2003; Miao et al., 2008; Xiao et al., 2009; Jian et al., 2010), the Erenhot-Hegenshan ophiolite belt (Sengör et al., 1993; Robinson et al., 1999), the Airgin Sum-Xilinhot area (Xu et al., 2014; Xu et al., 2015) or the Xar Moron suture zone (Wang and Fan, 1997; Li, 2006; Li et al., 2007; Miao et al., 2008; Wu et al., 2011; Liu et al., 2016; Li et al., 2019).

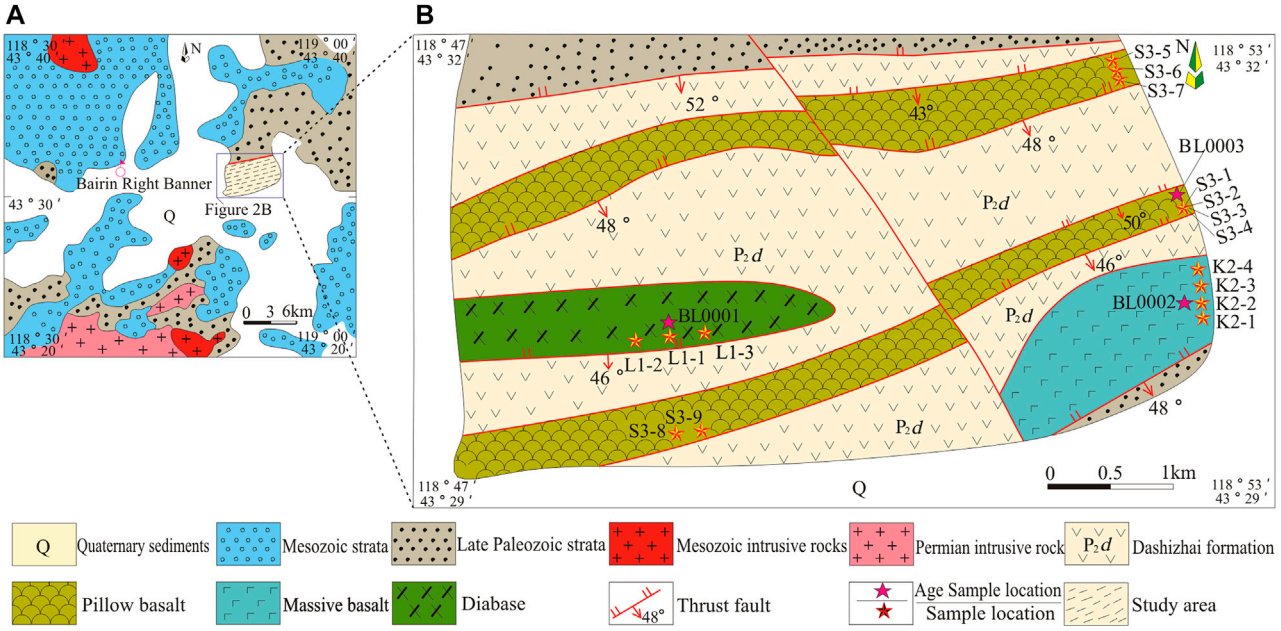

FIGURE 2
(A) Location of the study area. **(B)** Geological map in Bairin Right Banner, Inner Mongolia.

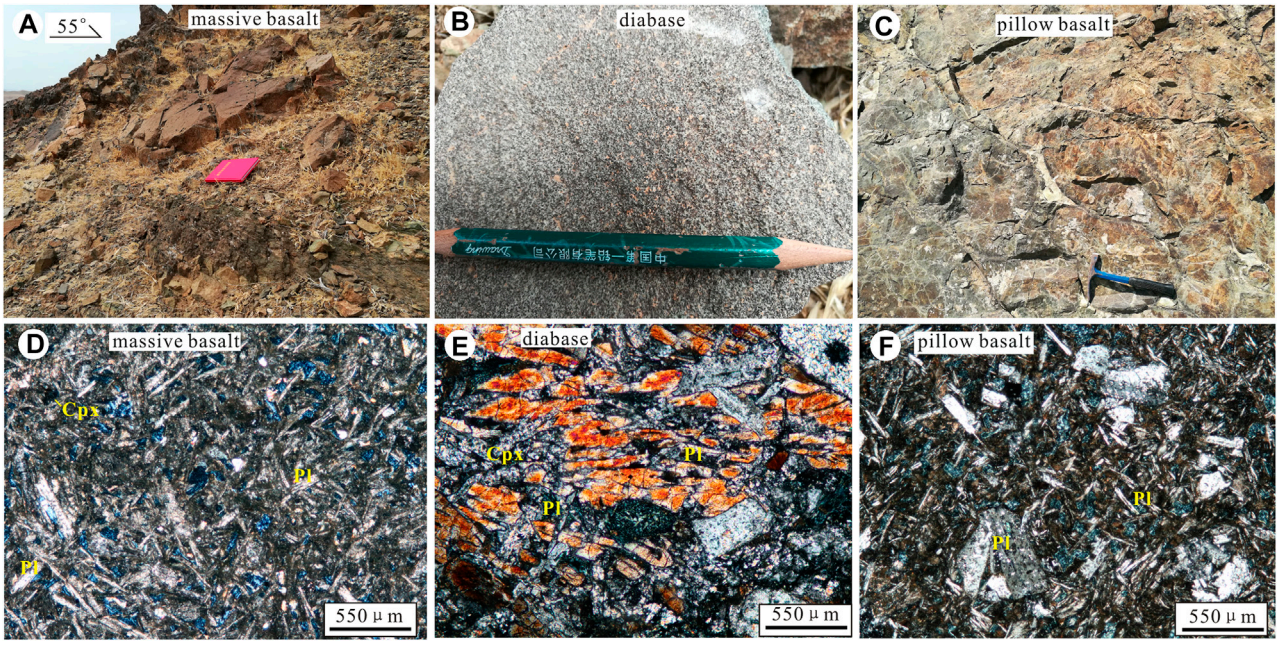

FIGURE 3
Representative photographs and photomicrographs (cross-polarized light) of the basic igneous rocks in the Bairin Right Banner area. **(A)** massive basalt outcrop; **(B)** diabase outcrop; **(C)** pillow basalt outcrop; **(D)** massive photomicrograph; **(E)** diabase photomicrograph; **(F)** pillow basalt photomicrograph; Cpx: Clinopyroxene; Pl: Plagioclase.

The ophiolite belts distributed in central Inner Mongolia can be divided into the Ondorsum ophiolite belt, Solonker-Mandula ophiolite belt, Kedanshan-Jiujingzi ophiolite belt (Xar Moron suture zone), Jiaoqier ophiolite belt, Daqing pasture-Diyanmiao ophiolite belt, and Erenhot-Hegenshan ophiolite belt (Figure 1B; Song et al., 2015; Li et al., 2019). In recent years, many researchers have carried out studies on geochronology, petrology, and petrogeochemistry of the ophiolites (Xiao et al., 2003; Miao et al., 2008; Jian et al., 2012; Liu et al., 2013; Song et al., 2015; Zhang et al., 2015; Zhou et al., 2015; Yang et al., 2017; Zhu et al., 2017), which have provided reliable geological data for the study of regional tectonic evolution. However, the situation of the Xar Moron suture zone is relatively conjectural due to limited research which restricts the comprehensive understanding of the time and location of the final

10.3389/feart.2023.1109206

TABLE 1 LA-ICP-MS zircon U-Pb data for the basic igneous rocks in Bairin Right Banner.

	Pb	Th	U	Th/U	207Pb/206Pb	207Pb/206Pb	207Pb/235U	207Pb/235U	206Pb/238U	206Pb/238U	207Pb/235U	207Pb/235U	206Pb/238U	206Pb/238U	207Pb/206Pb	207Pb/206Pb
	ppm	ppm	ppm		Ratio	1sigma	Ratio	1sigma	Ratio	1sigma	Age (Ma)	1sigma	Age (Ma)	1sigma	Age (Ma)	1sigma
Sample BL0001 Diabase																
Sample 01	6	71	87	0.82	0.053730	0.002328	0.359882	0.016847	0.048333	0.000529	305.6	12.8	305.1	3.5	315.8	95.5
Sample 02	8	121	140	0.87	0.056891	0.001454	0.468727	0.013150	0.059743	0.000684	384.4	10.2	375.4	4.2	443.3	53.0
Sample 03	6	56	111	0.50	0.053324	0.001843	0.412272	0.014256	0.055598	0.000564	343.6	12.3	342.6	3.6	342.8	77.2
Sample 04	4	60	55	1.10	0.086810	0.005754	0.433871	0.029245	0.036590	0.000458	365.4	22.6	303.7	3.9	1335.7	130.5
Sample 05	2	10	29	0.33	0.067647	0.012439	0.382386	0.057327	0.041490	0.000682	326.2	47.1	261.5	3.3	825.4	325.6
Sample 06	37	26	73	0.36	0.167455	0.001955	10.985318	0.155848	0.476413	0.005254	2520.7	34.1	2510.9	27.4	2530.3	20.4
Sample 07	24	146	295	0.49	0.056567	0.000754	0.586412	0.008640	0.076684	0.000769	467.4	5.9	472.3	5.0	461.0	27.7
Sample 08	21	200	410	0.49	0.053888	0.000888	0.357930	0.006634	0.047752	0.000539	305.2	5.5	300.5	3.5	325.0	38.2
Sample 09	11	87	231	0.38	0.095435	0.002245	0.381422	0.015587	0.042392	0.000476	484.0	10.3	259.8	2.9	1535.1	42.5
Sample 10	75	80	143	0.56	0.167677	0.001873	10.989427	0.186797	0.478752	0.006862	2521.5	40.9	2517.5	36.0	2525.5	19.0
Sample 11	6	132	106	1.25	0.057243	0.002778	0.337659	0.016264	0.042587	0.000438	288.8	14.2	262.7	2.5	497.1	106.6
Sample 12	62	72	107	0.68	0.179884	0.002125	12.482329	0.159740	0.513511	0.004886	2642.3	32.8	2629.9	25.6	2651.9	18.5
Sample 13	20	176	314	0.56	0.057663	0.000894	0.498864	0.008570	0.062843	0.000652	411.9	7.0	393.9	4.2	515.2	34.2
Sample 14	5	80	93	0.86	0.052862	0.002674	0.351179	0.017924	0.048136	0.000487	305.9	15.6	303.5	3.2	324.3	115.8
Sample 15	4	50	54	0.93	0.063478	0.004624	0.295592	0.028868	0.041615	0.000521	335.4	25.7	260.5	3.1	721.9	150.2
Sample 16	12	194	295	0.66	0.071683	0.002167	0.289945	0.013321	0.041321	0.000426	330.0	11.5	261.9	2.5	974.2	62.2

(Continued on following page)

10.3389/feart.2023.1109206

TABLE 1 (*Continued*) LA-ICP-MS zircon U-Pb data for the basic igneous rocks in Bairin Right Banner.

	Pb	Th	U	Th/U	207Pb/206Pb	207Pb/206Pb	207Pb/235U	207Pb/235U	206Pb/238U	206Pb/238U	207Pb/235U	207Pb/235U	206Pb/238U	206Pb/238U	207Pb/206Pb	207Pb/206Pb
	ppm	ppm	ppm		Ratio	1sigma	Ratio	1sigma	Ratio	1sigma	Age (Ma)	1sigma	Age (Ma)	1sigma	Age (Ma)	1sigma
Sample BL0002 Massive basalt																
Sample 01	60	101	242	0.42	0.087192	0.001080	2.790297	0.038927	0.232100	0.002644	1352.9	18.9	1345.5	15.3	1364.7	23.8
Sample 02	27	85	104	0.82	0.086902	0.001063	2.780111	0.038715	0.232023	0.002400	1350.2	18.8	1345.1	13.9	1358.3	23.6
Sample 03	64	288	362	0.79	0.071401	0.000831	1.587040	0.021824	0.161206	0.001666	965.1	13.3	963.5	10.0	968.9	23.7
Sample 04	41	57	133	0.43	0.108123	0.001219	4.358039	0.056475	0.292330	0.002877	1704.4	22.1	1653.2	16.3	1768.0	20.6
Sample 05	105	237	318	0.74	0.104730	0.001167	4.358575	0.058611	0.301838	0.003211	1704.5	22.9	1700.4	18.1	1709.6	20.5
Sample 06	56	78	149	0.52	0.124227	0.001398	5.926772	0.076487	0.346021	0.003385	1965.2	25.4	1915.6	18.7	2017.8	19.9
Sample 07	88	196	546	0.36	0.072533	0.000823	1.598918	0.020518	0.159877	0.001551	969.8	12.4	956.1	9.3	1000.9	23.0
Sample 08	124	159	248	0.64	0.166133	0.001855	9.852636	0.126888	0.430125	0.004259	2421.1	31.2	2306.3	22.8	2519.1	18.8
Sample 09	48	96	263	0.36	0.075135	0.000853	1.869321	0.024370	0.180444	0.001782	1070.3	14.0	1069.4	10.6	1072.1	22.8
Sample 10	73	99	466	0.21	0.071838	0.000831	1.601226	0.022612	0.161658	0.001812	970.7	13.7	966.0	10.8	981.4	23.6
Sample 11	10	11	62	0.18	0.072431	0.001407	1.618019	0.033454	0.162016	0.001830	977.2	20.2	968.0	10.9	998.1	39.5
Sample 12	116	31	468	0.07	0.107619	0.001200	3.783657	0.048305	0.254990	0.002493	1589.3	20.3	1464.2	14.3	1759.5	20.4
Sample 13	14	29	87	0.33	0.071736	0.001219	1.598672	0.030957	0.161630	0.001906	969.7	18.8	965.8	11.4	978.5	34.6
Sample 14	33	33	215	0.15	0.072023	0.000995	1.602042	0.028478	0.161324	0.002131	971.0	17.3	964.1	12.7	986.6	28.1
Sample 15	23	312	490	0.64	0.051918	0.000927	0.307934	0.006064	0.043017	0.000454	272.6	5.4	271.5	2.9	281.8	40.8
Sample 16	71	131	390	0.34	0.075899	0.000898	1.886762	0.025704	0.180294	0.001772	1076.4	14.7	1068.6	10.5	1092.4	23.7

(Continued on following page)

TABLE 1 (*Continued*) LA-ICP-MS zircon U-Pb data for the basic igneous rocks in Bairin Right Banner.

	Pb	Th	U	Th/U	207Pb/206Pb	207Pb/206Pb	207Pb/235U	207Pb/235U	206Pb/238U	206Pb/238U	207Pb/235U	207Pb/235U	206Pb/238U	206Pb/238U	207Pb/206Pb	207Pb/206Pb
	ppm	ppm	ppm		Ratio	1sigma	Ratio	1sigma	Ratio	1sigma	Age (Ma)	1sigma	Age (Ma)	1sigma	Age (Ma)	1sigma
Sample 17	86	269	891	0.30	0.059451	0.000672	0.799908	0.010601	0.097584	0.001009	596.8	7.9	600.2	6.2	583.7	24.5
Sample 18	54	48	349	0.14	0.072580	0.000827	1.607943	0.021601	0.160677	0.001667	973.3	13.1	960.5	10.0	1002.2	23.1
Sample 19	16	47	96	0.49	0.072640	0.001416	1.601324	0.033184	0.159882	0.001563	970.7	20.1	956.1	9.3	1003.9	39.6
Sample 20	90	86	267	0.32	0.152377	0.001695	6.555644	0.090066	0.312029	0.003447	2053.4	28.2	1750.7	19.3	2372.8	19.0
Sample 21	29	80	293	0.27	0.059839	0.000750	0.822486	0.012234	0.099687	0.001132	609.4	9.1	612.6	7.0	597.8	27.2
Sample 22	120	141	680	0.21	0.075677	0.000845	1.880435	0.025084	0.180217	0.001863	1074.2	14.3	1068.2	11.0	1086.5	22.4
Sample 23	12	179	282	0.63	0.051495	0.000906	0.306449	0.005839	0.043161	0.000444	271.4	5.2	272.4	2.8	263.0	40.4
Sample 24	48	156	154	1.01	0.095320	0.001093	3.493022	0.048380	0.265777	0.002924	1525.6	21.1	1519.3	16.7	1534.4	21.6
Sample 25	28	75	145	0.52	0.075612	0.000896	1.880655	0.026282	0.180393	0.001889	1074.3	15.0	1069.1	11.2	1084.8	23.7
Sample BL0003 Pillow basalts																
Sample 01	28	51	327	0.16	0.058938	0.000874	0.697610	0.013299	0.089076	0.001166	535.3	9.7	540.2	6.6	525.4	30.7
Sample 02	193	245	561	0.44	0.212370	0.001245	5.096361	0.065220	0.358289	0.004417	1835.8	24.5	1830.6	19.0	1838.3	20.3
Sample 03	23	242	438	0.55	0.054251	0.000756	0.382916	0.006854	0.051786	0.000488	321.9	5.2	320.0	3.1	335.2	32.6
Sample 04	19	227	459	0.49	0.052910	0.000898	0.293892	0.005453	0.041643	0.000415	258.2	4.9	256.8	3.6	281.4	39.6
Sample 05	7	55	116	0.48	0.053917	0.001659	0.382266	0.013652	0.052885	0.000551	322.6	9.8	320.9	4.4	324.3	73.6
Sample 06	16	263	286	0.92	0.054126	0.000977	0.373595	0.007524	0.051978	0.000545	322.5	6.5	321.5	3.4	329.0	41.3
Sample 07	9	119	213	0.56	0.065659	0.003243	0.388415	0.013357	0.044357	0.000454	331.9	11.5	256.8	2.8	784.9	71.5

(Continued on following page)

10.3389/feart.2023.1109206

TABLE 1 (*Continued*) LA-ICP-MS zircon U-Pb data for the basic igneous rocks in Bairin Right Banner.

	Pb	Th	U	Th/U	207Pb/206Pb	207Pb/206Pb	207Pb/235U	207Pb/235U	206Pb/238U	206Pb/238U	207Pb/235U	207Pb/235U	206Pb/238U	206Pb/238U	207Pb/206Pb	207Pb/206Pb
	ppm	ppm	ppm		Ratio	1sigma	Ratio	1sigma	Ratio	1sigma	Age (Ma)	1sigma	Age (Ma)	1sigma	Age (Ma)	1sigma
Sample 08	11	152	225	0.68	0.053314	0.001753	0.292122	0.009929	0.041650	0.000426	261.2	8.7	257.8	2.7	291.4	76.5
Sample 09	7	71	98	0.73	0.053879	0.003171	0.373292	0.022117	0.053185	0.000535	322.3	18.0	320.8	3.5	325.6	132.9
Sample 10	34	388	621	0.62	0.053447	0.001332	0.378866	0.008599	0.052129	0.000574	317.8	7.4	321.5	3.5	304.6	57.2
Sample 11	11	106	194	0.54	0.053219	0.001439	0.373787	0.014243	0.051995	0.000598	321.6	12.5	320.5	3.6	330.5	60.6
Sample 12	9	198	215	0.92	0.052612	0.002276	0.291270	0.013346	0.042770	0.000425	258.5	10.0	257.5	2.5	266.8	95.8
Sample 13	71	71	533	0.13	0.069490	0.000787	1.314753	0.016776	0.146563	0.001333	848.8	11.8	825.2	7.5	911.6	23.5
Sample 14	20	243	532	0.46	0.052450	0.000813	0.286295	0.005188	0.042329	0.000455	256.5	5.5	255.9	2.8	261.6	35.3
Sample 15	34	368	639	0.58	0.065153	0.001134	0.431248	0.009299	0.048169	0.000543	363.0	7.7	303.7	3.5	776.5	36.5
Sample 16	10	123	195	0.63	0.053951	0.001986	0.372929	0.015722	0.051943	0.000546	321.3	12.6	322.3	3.5	327.7	85.7

10.3389/feart.2023.1109206

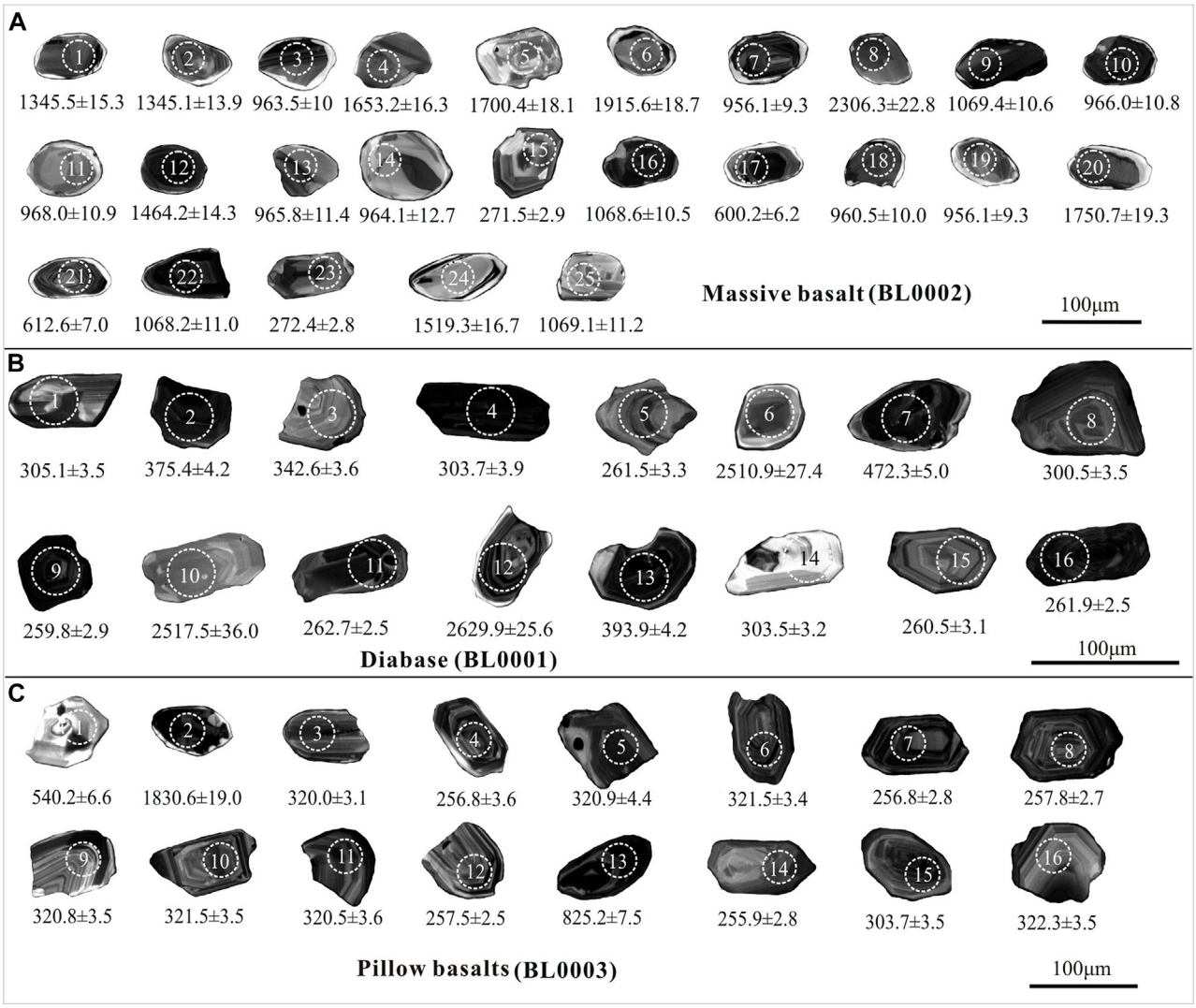

FIGURE 4
Cathodoluminescence images of zircons from basic igneous rocks in the Bairin Right Banner area, Inner Mongolia. **(A)** massive basalt (BL0002); **(B)** diabase (BL0001); **(C)** pillow basalt (BL0003).

collision between the Siberian and the North China plates. In this study, based on regional geological surveys and a detailed laboratory comprehensive study, we for the first time identified newly discovered basic igneous rocks in Bairin Right Banner, Inner Mongolia, and carried out petrology, geochemistry, and LA-ICP-MS zircon U-Pb isotope geochronological studies with the aim to establish their genesis and geodynamic setting. Our results have robust implications for the evolution of the Paleo-Asian Ocean, the time and location of the final suturing, and the regional tectonic evolution of the Siberian and the North China plates.

2 Regional geology and petrographic features

2.1 Regional geology

The Xar Moron suture zone is located in the Eastern part of the Ondor Sum subduction accretion complex belt, consisting mainly of Kedanshan (Jian et al., 2008; Zhang et al., 2015), Xingshuwa (Song et al., 2015), Banlashan (Miao et al., 2008), and Jiujingzi (Liu et al., 2016) ophiolite fragments, which are distributed along the northern edge of the Xar Moron River in an east-west direction. The main rock types include serpentine peridotite, pyroxenite, gabbro, chert, and metamorphosed basalt. Most of them are isolated blocks in structural contact with the surrounding rock (Wang and Fan, 1997; Li et al., 2007; Liu et al., 2016). The Southern part of the study area is the Bainaimiao arc belt, while the Northern part is the Ondor Sum subduction accretion complex belt (Figure 1B; Xiao et al., 2003; Li et al., 2019). From the Paleozoic to the Mesozoic, a series of intense calc-alkaline magmatic activities and marine volcano-sedimentary strata occurred (Li et al., 2007; Zhang et al., 2009; Song et al., 2015; Liu et al., 2016; Li et al., 2019). The Middle Permian Dashizhai Formation (P_2d) is mainly composed of intermediate-acid volcanic rocks and pyroclastic rocks. The Middle Permian Zhesi Formation (P_2zs) is a combination of sandstone slate with limestone lenticular bodies in neritic and littoral facies, abundant in fossils such as brachiopods. The Upper Permian Linxi Formation (P_3l) is mainly composed of

sandstone and slate, while continental sedimentary strata were formed in the Late Permian (Zhang et al., 2014; Liu et al., 2016).

2.2 Petrographic features of the basic igneous rocks

The newly discovered basic igneous rocks are located about 12 km east of Bairin Right Banner, Inner Mongolia (Figure 2A). These rocks are in fault contact with the Late Paleozoic sedimentary formation and the Middle Permian Dashizhai Formation, which are covered by Quaternary sediments. These basic igneous rocks were intruded by a few diorite porphyrite dikes and quartz dikes. The rock types mainly include pillow basalt, diabase, and massive basalt (Figure 2B). The strike of the fault varies from 300°–360°, with a dip angle ranging from 40°–55°.

The massive basalt is gray-black to black-green and, due to weathering, shows a gray-brown color, with a porphyritic massive structure (Figure 3A). Plagioclase phenocryst (varying from 5% to 12%) is euhedral, narrow platy surrounded by a vitreous microcrystalline plagioclase matrix. The particle size of plagioclase phenocryst varies from 0.1 mm to 0.5 mm. Mafic minerals are mostly altered into epidote and chlorite (Figure 3D).

The diabase is dark gray and, due to weathering, shows a grey-black color, with massive structures (Figure 3B). The rock is composed of plagioclase (varying from 62% to 68%) and pyroxene (varying from 32% to 38%). The plagioclase is subhedral platy columnar, with grain size varying from 0.3 mm to 1.2 mm. Pyroxene is granular, columnar, light brown, shows high protrusion, fills the gaps in plagioclase (Figure 3E), and has second-order interference colors with particle sizes varying from 0.4 mm to 1.1 mm.

The pillow basalt appears gray-green but its color when weathered is mostly black-green and gray-brown. Weathering-induced small carbonate cracks are observable and the rocks show pillow structures (Figure 3C). The pillow structures are relatively well-preserved, displaying elliptic, spherical, and renal shapes with varying sizes ranging from 25 cm to 65 cm wide and 100 cm to 150 cm long. The basic plagioclase (varying from 3% to 10%) phenocrysts are euhedral platy, showing twining, and cleavages, with vitreous microcrystalline plagioclase matrix. The plagioclase microcrystals are elongated and show a hollow skeleton crystal structure. Particle size ranges from 0.1 mm to 0.5 mm, and the microcrystalline spaces are mostly filled by vitreous materials (Figure 3F).

3 Samples and methods

For whole-rock geochemical analysis, four representative samples (K2-1–K2-4) of massive basalt, three representative samples (L1-1 to L1-3) of diabase, and nine representative samples (S3-1 to S3-9) of pillow basalt were collected from the Bairin Right Banner area (Figure 2B). All the samples were used to conduct different analyses. Among them, a sample (BL0002) of massive basalt (BL0002), a sample (BL0001) of diabase, and a sample (BL0003) of pillow basalt were selected for LA-ICP-MS zircon U-Pb dating analysis. The sampling locations are shown in Figure 2B. The coordinates of the samples of massive basalt (BL0002), diabase (BL0001), and pillow basalt (BL0003) are (43°30′32″ N, 118°53′03″ E), (43°29′55″ N, 118°52′10″ E), and (43°30′35″ N, 118°25′56″ E), respectively.

3.1 LA-ICP-MS zircon U–Pb analysis

LA-ICP-MS zircon U-Pb geochronological analysis was done in the State Key Laboratory of Geological Processes and Mineral Resources, China University of Geosciences. The instrument used for the analyses was an Analyte Excite ICP-MS of Teledyne Cetac Technologies Co., Ltd. with a matching New Wave UP 193 laser ablation system. The diameter of the laser ablation spot beam was 32 μm, with 20 μm–40 μm laser ablation depth. The internationally accepted standard zircon GJ-1 was used as the external standard for age calculation, and the element content was corrected by NIST SRM610, a silicate glass synthesized by the National Bureau of Standards and Materials, and ^{29}Si was used as the internal standard element (Liu et al., 2010a; Hu et al., 2011). The data processing was done by ICPMSDataCal 8.4 program (Liu et al., 2010a, b), while age calculation and concordant diagrams were done using ISOPLOT ver. 3.0 (Ludwig, 2003; Yuan et al., 2004). U-Pb dating results are shown in Table 1.

3.2 Major and trace element analyses

The major elements, rare earth elements, and trace elements of the rocks were analyzed in the Analysis and Testing Research Center at the Beijing Institute of Geology, Nuclear Industry. The major element analysis instrument was a Philips PW2404 X-ray fluorescence spectrometer (XRF), with an analysis deviation of 1%–5%. The analytical instrument for trace elements and rare earth elements was a Finnigan MAT Element I high-resolution plasma mass spectrometer (HR-ICP-MS), with an analytical deviation of 1%–3%. The test basis and method refer to DZ/T0223-2001 inductively coupled plasma mass spectrometry (ICP-MS), with a room temperature of 20°C and relative humidity of 30% during the test. The international standards AGV-1, BHVO-1, and BCR-1 were used to calibrate the element concentration of the samples (Li et al., 2002). The results of the analyses of major and trace elements are shown in Supplementary Table S1.

4 Analytical results

4.1 Zircon U-Pb ages

Twenty-five zircon grains with grain sizes ranging from 50 μm–100 μm long and length-to-width ratios ranging from 1:1 to 2:1 from the massive basalt were analyzed (Figure 4A). The zircon U-Pb ages yielded two groups of age suits ranging from 2306.3 ± 22.8 Ma to 271.5 ± 2.9 Ma. The first group contains twenty-three zircons grains, and ages were traddled on or near the concordant curve (Figure 5A) on the concordant diagram. Zircon grains varied in size, and most of them were rounded-sub-rounded. The cathodoluminescence images were translucent-transparent, while some were black. Some zircon grains showed inherited cores, and some of them had zonal structures, showing the characteristics of captured zircon, with Th/U ratios ranging from 0.07 to 1.01. Except for

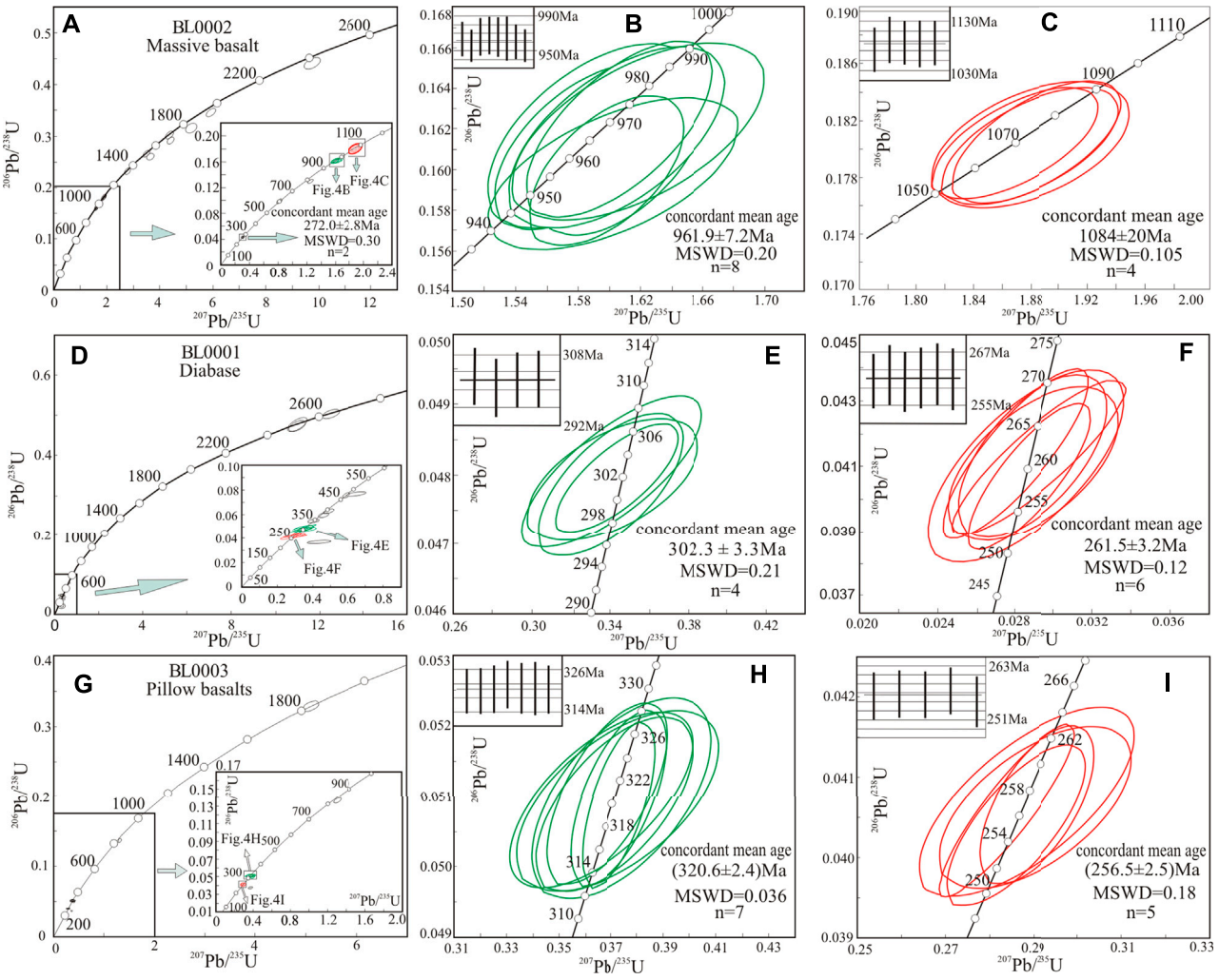

FIGURE 5
Concordia U-Pb diagrams of zircons from basic igneous rocks in the Bairin Right Banner area, Inner Mongolia. **(A–C)** massive basalt (BL0002); **(D–F)** diabase (BL0001); **(G–I)** pillow basalt (BL0003).

one zircon grain (No. 12), all the other Th/U ratios were >0.1, which showed the characteristics of magmatic zircon (Corfu et al., 2003; Wu and Zheng, 2004). There were thirteen $^{207}Pb/^{206}Pb$ zircons older than 1Ga, the oldest $^{207}Pb/^{206}Pb$ age was 2519.1 ± 18.8 Ma, and the youngest $^{206}Pb/^{238}U$ age was 600.2 ± 6.2 Ma. Two obvious peak intervals existed in this age group. The zircons yielding the concordant mean ages of 961.9 ± 7.2 Ma (MSWD = 0.20, *n*=8) and 1084 ± 20 Ma (MSWD = 0.105, *n* = 4) were the captured zircons (Figures 5B, C). Zircons No. 15 and No. 23 were transparent-translucent, short-columnar-long-columnar, had relatively perfect crystallization, and wide magmatic oscillatory zoning, with Th/U ratios between 0.63 and 0.64, showing the characteristics of magmatic zircon (Corfu et al., 2003; Wu and Zheng, 2004). The concordant mean age of 272.0 ± 2.8 Ma (MSWD = 0.30, *n* = 2) represented the formation age of massive basalt (Figure 5A).

Sixteen zircons with grain sizes ranging from 60 μm to 110 μm long and length-to-width ratios ranging from 1:1 to 3:1 from diabase were analyzed (Figure 4B). The grains varied in size, were rounded, columnar, and angular, and most of them were relatively developed. The U-Pb ages ranged from 2629.9 ± 25.6 Ma to 235.7 ± 3.9 Ma, and could be divided into three groups according to the crystal morphology and internal structure of zircon (Figure 5D). The first group contained seven zircon grains, of which 2629.9 ± 25.6 Ma, 2517.5 ± 36.0 Ma, and 2510.9 ± 27.4 Ma were the oldest ages, while the other $^{206}Pb/^{238}U$ ages ranged from 472.3 ± 5.0 Ma to 342.6 ± 3.6 Ma. The zircon grains were rounded and irregular in morphology, and the cathodoluminescence images were transparent and translucent in color. Some of them had inherited cores and weak bands. Most of the zircon grains were irregularly fractured residues, which were characteristic of captured zircon. The second group contained four zircon grains, the $^{206}Pb/^{238}U$ ages ranged from 305.1 ± 3.5 Ma to 303.3 ± 3.1 Ma, and the Th/U ratios varied from 0.82 to 1.10, indicating the characteristics of magmatic zircon (Corfu et al., 2003; Wu and Zheng, 2004). The cathodoluminescence images were transparent and translucent, while some images were dark. Some zircons had inherited cores, some had weak zones, and most were irregularly fractured residues; the zircon grains were relatively small, which indicated they might have been captured by magma during an eruption. These zircons in the second group yielded a concordant mean age of 302.3 ± 3.3 Ma (MSWD = 0.21, *n* = 4)

(Figure 5E). The zircons in the third group were transparent-translucent, with euhedral platy morphology and relatively perfect crystallization, exhibiting well-developed wide oscillatory zoning. The $^{206}Pb/^{238}U$ ages varied from 262.7 ± 2.5 Ma to 259.8 ± 2.9Ma, The Th/U ratios were in the ranges of 0.33–1.25, showing the characteristics of magmatic zircon (Corfu et al., 2003; Wu and Zheng, 2004). These zircons yielded a concordant mean age of 261.5 ± 3.2 Ma (MSWD = 0.12, n = 6), which represented the formation age of diabase (Figure 5F).

Sixteen zircon grains with grain sizes ranging from 50 μm–100 μm long and length-to-width ratios ranging from 1:1 to 2:1 from pillow basalt were analyzed (Figure 4C). The zircon grains varied in size, and most of them showed rounded and broadly platy morphology. The zircon U-Pb ages ranged from 1830.6 ± 19.0 Ma to 255.9 ± 2.8 Ma, and could be divided into three groups according to the crystal morphology and internal structure of zircon (Figure 5G). In the first group, the zircon ages were 1830.6 ± 19.0 Ma, 825.2 ± 7.5 Ma, and 540.2 ± 6.6 Ma, and the zircon grains were relatively small, rounded, and irregular, with inherited cores. Some weak bands and dark cathodoluminescence images showed the characteristics of captured zircon. In the second group, the ages of $^{206}Pb/^{238}U$ varied from 322.3 ± 3 Ma to 303.7 ± 3.5 Ma, and the Th/U ratios varied from 0.48 to 0.92, indicating the characteristics of magmatic zircon (Corfu et al., 2003; Wu and Zheng, 2004). These zircons mainly occurred as euhedral-subhedral grains, with transparent and translucent cathodoluminescence images, and some of them showed inherited cores and zoning. Most of the zircon grains were relatively small and irregularly fractured, which indicated they might have been captured by magma during an eruption. The zircons in the second group produced a concordant mean $^{206}Pb/^{238}U$ age of 320.6 ± 2.4 Ma (MSWD = 0.036, n = 7) (Figure 5H). The zircons in the third group were transparent-translucent with euhedral platy morphology, had relatively perfect crystallization, and exhibited well-developed wide oscillatory zoning. The Th/U ratios were between 0.46 and 0.92, which showed the characteristics of magmatic zircon (Corfu et al., 2003; Wu and Zheng, 2004). These zircons in the third group yielded a concordant mean $^{206}Pb/^{238}U$ age of 256.5 ± 2.5 Ma (MSWD = 0.18, n = 5), which represented the formation age of pillow basalt (Figure 5I).

4.2 Major element geochemistry

The SiO_2 contents of massive basalt, diabase, and pillow basalt ranged from 45.76–51.56 wt% (average 48.84 wt%, Supplementary Table S1). Their TiO_2 contents ranged from 0.97–1.79 wt% (average 1.39 wt%) with MgO contents ranging from 5.08–11.95 wt % (average 6.72 wt%) and $Mg^{\#}$ values ranging from 53.5–71.0. Their Na_2O contents (2.07–5.24 wt%, average 3.43 wt%) were higher than K_2O contents (0.17–0.92 wt%, average 0.51 wt%). The Al_2O_3 contents of pillow basalt ranged from 16.76–17.62 wt% (average 17.14 wt%), which represented high alumina basalt (>16.5 wt%, Crawford et al., 1987). Their TiO_2 contents varied between island arc tholeiite (average 0.8 wt%) and mid-ocean ridge basalt (average 1.5 wt%) (Sun and McDonough, 1989), and their $Mg^{\#}$ values were lower than that of mantle-derived magma (68–72, Frey et al., 1978). Loss on ignition (LOI) of the rock samples ranged from 0.66 to 4.58 wt%, which was affected by minor additions of seawater or fluid alteration. Consequently, the relatively stable high-field strength elements such as Nb, Ce, Zr, and Y (Pearce and Cann, 1973) were selected to classify the rock types. In the Zr/TiO_2-Nb/Y diagram (Figure 6A), massive basalt, diabase, and pillow basalt samples are plotted on the boundary between subalkaline basalt and andesite/basalt. In the SiO_2-FeO^T/MgO diagram (Figure 6B), all the rock samples fell in the field of the tholeiite series.

4.3 Trace element geochemistry

The sum of the total contents of REEs (ΣREE) of the massive basalt, diabase, and pillow basalt samples ranged from 50.50–100.56 × 10^{-6} (average 79.49 × 10^{-6}). Their ΣREE were in between those of oceanic island basalt (OIB, 198.96 × 10^{-6}) and enriched mid-ocean ridge basalt (E-MORB, 49.09 × 10^{-6}), and close to E-MORB. Their $(La/Yb)_N$ values and δEu values ranged from 1.80–3.25 and 0.95–1.14, respectively. In the chondrite normalized rare earth element (REE) diagrams (Figure 7), their REEs patterns were characterized by slightly LREE-enrichment and nearly flat HREE like that of E-MORB, with the slightly positive Eu anomalies. In the primitive mantle-normalized incompatible element diagrams (Figure 7), the massive basalt and diabase samples were relatively enriched in large ion lithophile elements (LILEs) (e.g., Rb, Ba, and U), while depleted in high field strength elements (HFSEs) (e.g., Nb, Ta). The pillow basalt samples were relatively depleted in Rb and Th and enriched in Ba and U.

5 Discussion

5.1 Implications of zircon U-Pb ages

The analyzed zircons from the samples of the massive basalt, diabase, and pillow basalt exhibited a wide range of ages, i.e., 2629.9 ± 25.6 Ma to 255.9 ± 2.8 Ma. Consequently, we collected a set of recently published zircon ages to compare with the ages obtained in this study for better interpretation (Figure 8). Based on the age data, we argued that the zircon grains might have been derived from various sources. The zircons yielding ages greater than 1 Ga might have been sourced from the North China Craton (NCC) (Zhao et al., 2000; Lu et al., 2020), while zircon grains of ages from 1 Ga to 600 Ma might have been sourced from Precambrian micro-massif in the adjacent area, which is considered as an important tectonic feature of the Xingmeng orogenic belt to the north of the NCC (Rojas-Agramonte et al., 2011; Xu et al., 2013; Zhang et al., 2013; Song et al., 2015). In addition, the zircons yielding 600 Ma-472 Ma ages have probably been sourced from the adjacent early Paleozoic Island arc magmatic rocks (Jian et al., 2008; Li et al., 2012; Zhou et al., 2012).

The U-Pb age data of the adjacent areas (Figure 8A) showed three distinct intervals: 490–405 Ma, 360–270 Ma, and 250–200 Ma (Yang et al., 2018; Lu et al., 2020). The age range of 490–405 Ma and 360–270 Ma represents the early-late Paleozoic Island arc magmatic events in the region (Lu et al., 2020; Yang et al., 2022). These events produced the volcanic rocks of the Dashizhai Formation (Yang et al., 2018), basic-ultrabasic rocks of the Xilinhot massif (Lu et al., 2020), and the early Paleozoic Island arc-related rocks of Sonidzuoqi-Xiwuqi (Jian et al., 2008), which are widely distributed in the north of the study area. The concordant mean ages of 302.3 ± 3.3 Ma and 320.6 ± 2.4 Ma yielded by diabase and pillow basalt samples, respectively, reflect large-scale magmatic events during the Carboniferous-Permian

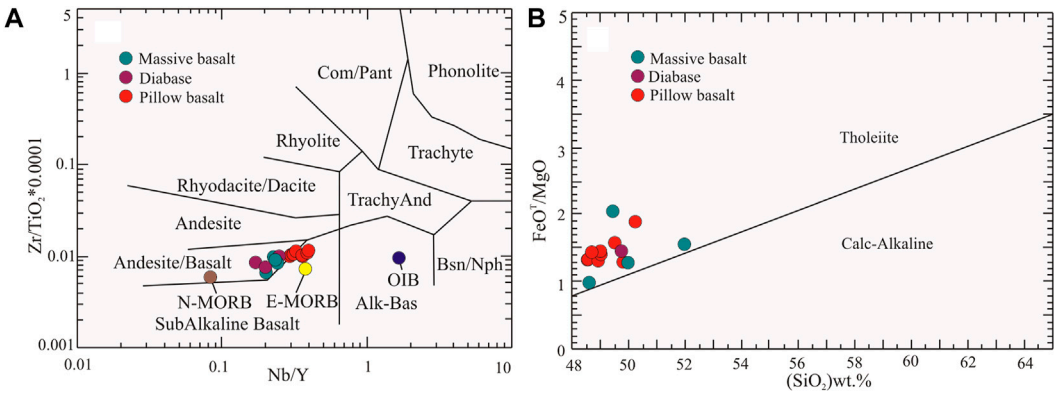

FIGURE 6
(A) Zr/TiO_2-Nb/Y diagram (Winchester and Floyd, 1977) and **(B)** SiO_2-FeO^T/MgO diagram (Miyashiro, 1974) of the basic igneous rocks in the Bairin Right Banner area, Inner Mongolia. Abbreviations: N-MORB, Normal mid-ocean ridge basalt; E-MORB, Enriched mid-ocean ridge basalt; OIB, oceanic island basalt; values are from Sun and McDonough, (1989).

(360–270 Ma) in the region (Song et al., 2015; Liu et al., 2016; Zhang et al., 2016; Liu et al., 2022). The concordant mean ages of the samples of massive basalt, diabase, and pillow basalt were 272.0 ± 2.8 Ma, 261.5 ± 3.2 Ma, and 256.5 ± 2.5 Ma, respectively; these ages, in conjunction with the ages of the gabbro in the Banlashan area (256 Ma, Miao et al., 2008) and the O-type adakitic andesite in the Bairin Right Banner area (257 Ma, Yang et al., 2018), represent intensive Late Permian magmatic activity. The age range of 250–200 Ma can be interpreted as the regional syn-to post-collisional magmatic events, i.e., Shuangjingzi granites (Li et al., 2007), Jianshetun granites (Liu et al., 2016), and Triassic granitic intrusions in the northern margin of the NCC (Zhao et al., 2019; Jing et al., 2022).

5.2 Magma source

The massive basalt, diabase, and pillow basalt samples showed low SiO_2 (up to 51.56 wt%), high MgO (up to 11.95 wt%), and $Fe_2O_3^T$ (up to 17.85 wt%) (Supplementary Table S1), suggesting that their precursor magma was sourced from the mantle. However, their $Mg^{\#}$ values were lower than those of mantle-derived magma (68–72, Frey et al., 1978), indicating the fractionation of their precursor magma during the evolution process. All the rock suits displayed slightly positive Eu anomalies (δEu = 0.95–1.14), indicating absence or minor plagioclase fractionation. In addition, the precursor melts of the studied rocks were contaminated by crustal materials during upwelling, as indicated by the presence of xenocrystic zircons. But the δCe values ranged from 0.88 to 1.01 ($\delta Ce=Ce_N/(La_N \times Pr_N)^{1/2}$), which were consistent with the range of δCe values of the rocks lacking crustal contamination (0.9–1.1, Polat and Hofmann, 2003). Also, the negative Th anomalies in the primitive mantle-normalized incompatible element diagrams (Figure 7) did not support significant crustal contamination. However, combined with the zircon ages obtained in this study, we argue that crustal contamination occurred to a certain extent during the formation of these rocks. The massive basalt and diabase displayed similar trace element patterns, i.e., enriched in Rb, Ba, and U, and depleted in Nb and Ta (Figure 7), suggesting the same magma source with the addition of subduction material (Pearce, 1982; Xie et al., 2016).

High field strength elements, such as Nb, Ta, Zr, Hf, Th, and HREE, were not easily affected by late-stage hydrothermal alteration and metamorphism during the magma evolution process (Pearce and Cann, 1973); consequently, these elements could distinguish the magma source and tectonic environment of the rocks. The Sm/Yb-Sm diagram (Figure 9A) shows that the massive basalt, diabase, and pillow basalt might have been produced as a result of a 10%–20% partial melting of spinel lherzolite mantle. Their partial melting curves deviated from DMM (depleted mantle) and were close to WAM (western Anatolia mantle), indicating that there was no single source of the depleted mantle (Aldanmaz et al., 2000). The U/Th-Th/Nb diagram (Figure 9B), shows that the massive basalts, diabases, and pillow basalts have similar magmatic sources as Izu-Bonin back-arc basalts (Xie et al., 2016), which are located near the source of the depleted mantle and contaminated by minor crustal contamination. The low U/Th values of some samples of the massive basalt, diabase, and pillow basalt suggest that they interacted with subduction plate fluids as well as the melt formed from subducting sediments. Combined with previous studies on the Nd and Sr isotopes (εNd (t) = 2.5–5) of intermediate-basic volcanic rocks in the Xilinhot and Xingshuwa areas (Miao et al., 2008; Song et al., 2015) and high-Mg andesite in the Linxi area (249 Ma, Zhang et al., 2009), we argue that the formation of massive basalt, diabase, and pillow basalt is closely related to the subduction-related depleted mantle. However, the genesis of massive basalt, diabase, and pillow basalt in this study is not supported by effective Sr, Nd, and Hf isotopic data, which must be focused on in future studies.

5.3 Tectonic environment

In the Hf/3-Th-Nb/16 diagram (Figure 10A), massive basalts are plotted in the transition field between enriched mid-oceanic ridge basalt (E-MORB) and calk-alkaline basalt (CAB), while the diabase samples (except one sample) are plotted in the island arc tholeiite (IAT) field, and pillow basalts are straddled across the E-MORB field. In the V-Ti diagram (Figure 10B), all of these rock samples are plotted

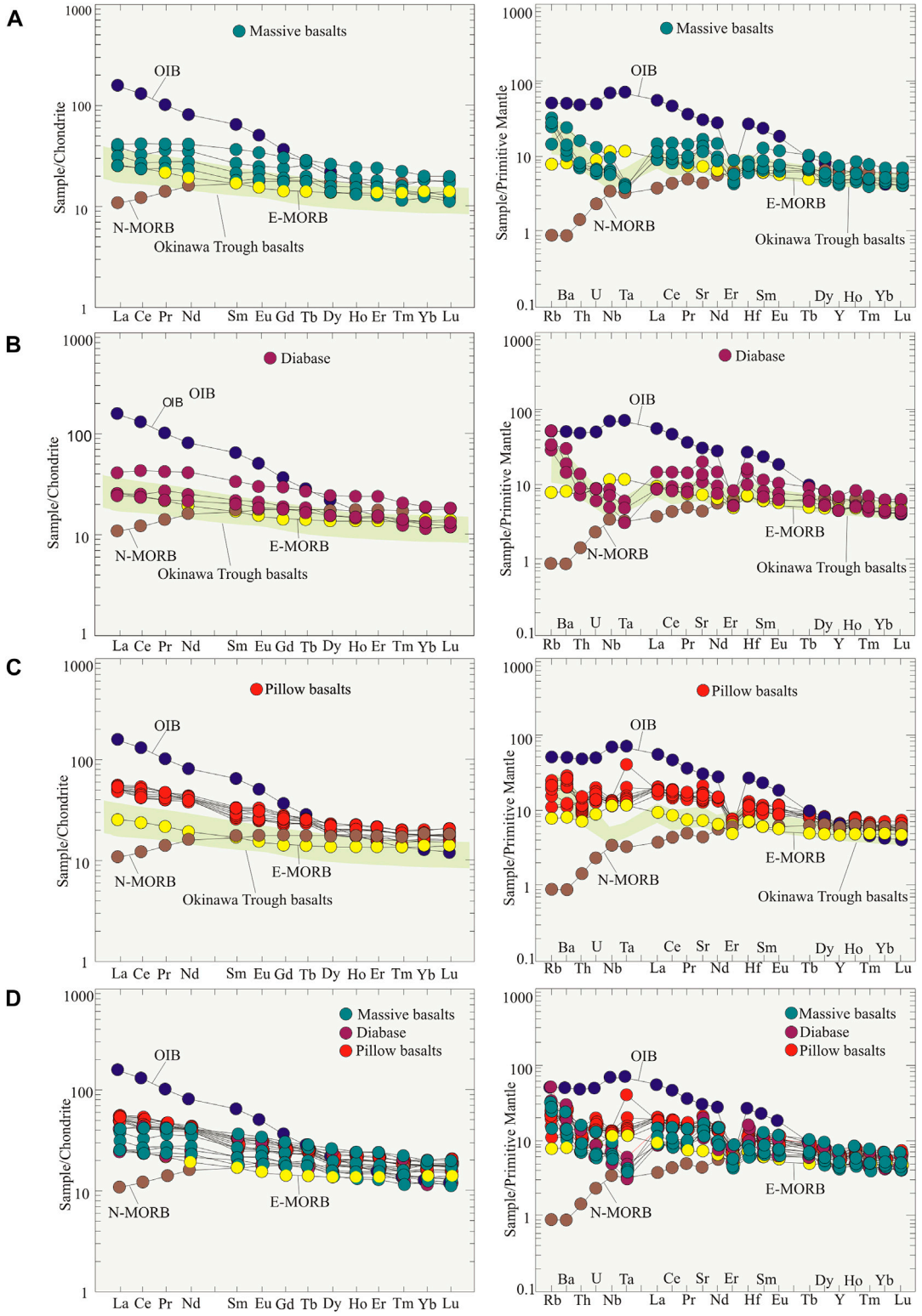

FIGURE 7
Rare earth element (REE) patterns and primitive mantle-normalized incompatible element diagrams of the basic igneous rocks in the Bairin Right Banner area, Inner Mongolia. Chondrite and primitive mantle-normalized values are from Boynton, (1984); Sun and McDonough, (1989), respectively; Normal Mid-Ocean Ridge Basalt (N-MORB), Enriched Mid-Ocean Ridge Basalt (E-MORB) and Ocean Island Basalt (OIB) values are from Sun and McDonough, (1989). **(A)** massive basalts; **(B)** diabases; **(C)** pillow basalts; **(D)**. Basic igneous rocks in Bairin Right Banner.

in genetic fields of the mid-ocean ridge basalt (MORB) and back-arc basin basalt (BABB). In the Ti-Zr diagram (Figure 10C), massive basalts and diabases show the properties of both MORB and calk-alkaline basalt (CAB), while all pillow basalt samples are plotted in the MORB field. In the Th/Yb-Ta/Yb diagram (Figure 10D), massive basalts and diabases fall in the ocean island arc field, and show the

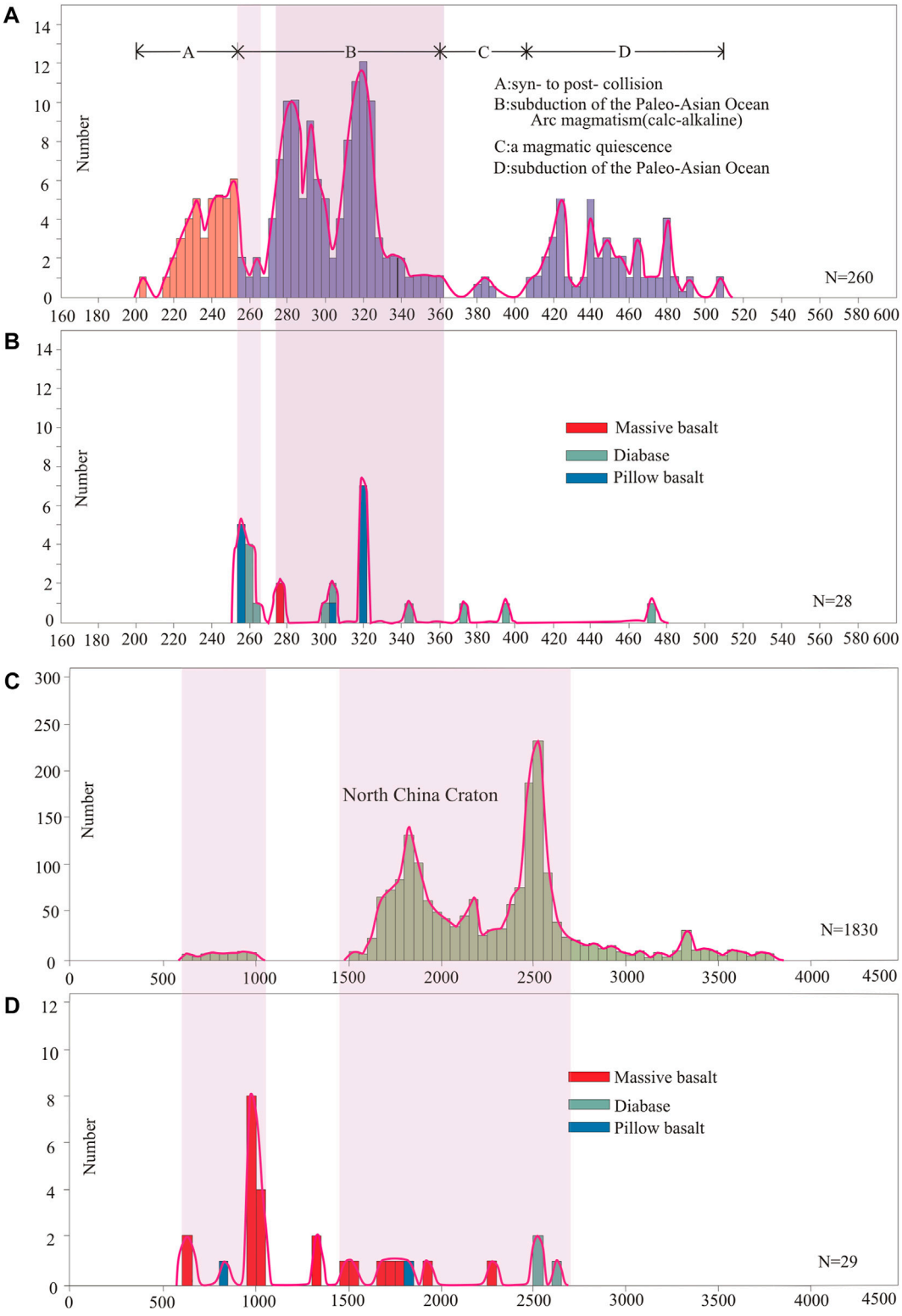

FIGURE 8
(A) Age spectrums of the adjacent areas (values are from Miao et al., 2008; Song et al., 2015; Lu et al., 2020); **(B)** Age spectrums of the study area; **(C)** Age spectrums of the North China Craton (after Lu et al., 2020); **(D)** Age spectrums of the study area.

characteristics of tholeiite-calc-alkaline transition. In addition, they were relatively enriched in large ion lithophile elements (e.g., Rb, Ba and U) and depleted in high field strength elements (e.g., Nb and Ta), which indicates that the formation of these rocks was influenced by subduction fluid (Condie, 1989; Song et al., 2015). The pillow basalts are plotted near E-MORB, close to the oceanic island arc field.

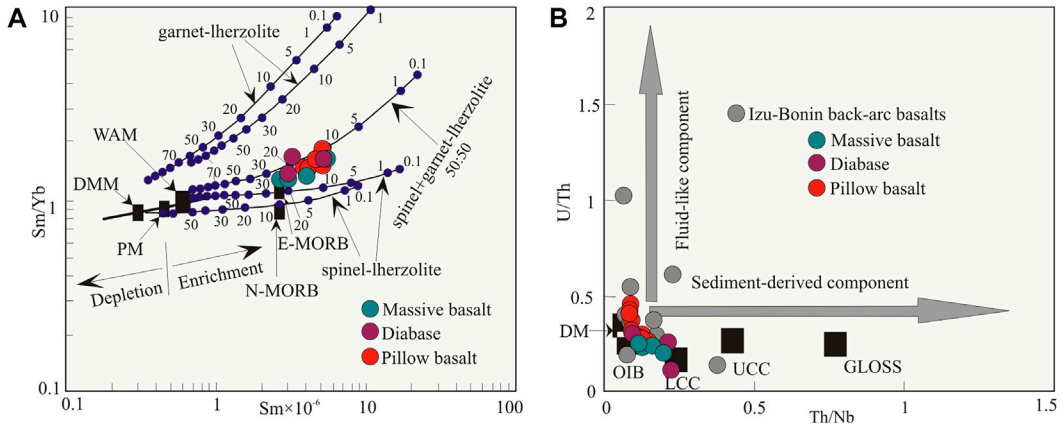

FIGURE 9
(A) Sm/Yb-Sm diagram (Aldanmaz et al., 2000) and **(B)** U/Th-Th/Nb diagram (Xie et al., 2016) of the basic igneous rocks in the Bairin Right Banner area, Inner Mongolia. Abbreviations: N-MORB, normal mid-ocean ridge basalt; E-MORB, enriched mid-ocean ridge basalt; DMM and DM, depleted mantle; WAM, western Anatolia mantle; UCC, upper continental crust; LCC, lower continental crust; PM, primitive mantle; GLOSS, global subducting sediment.

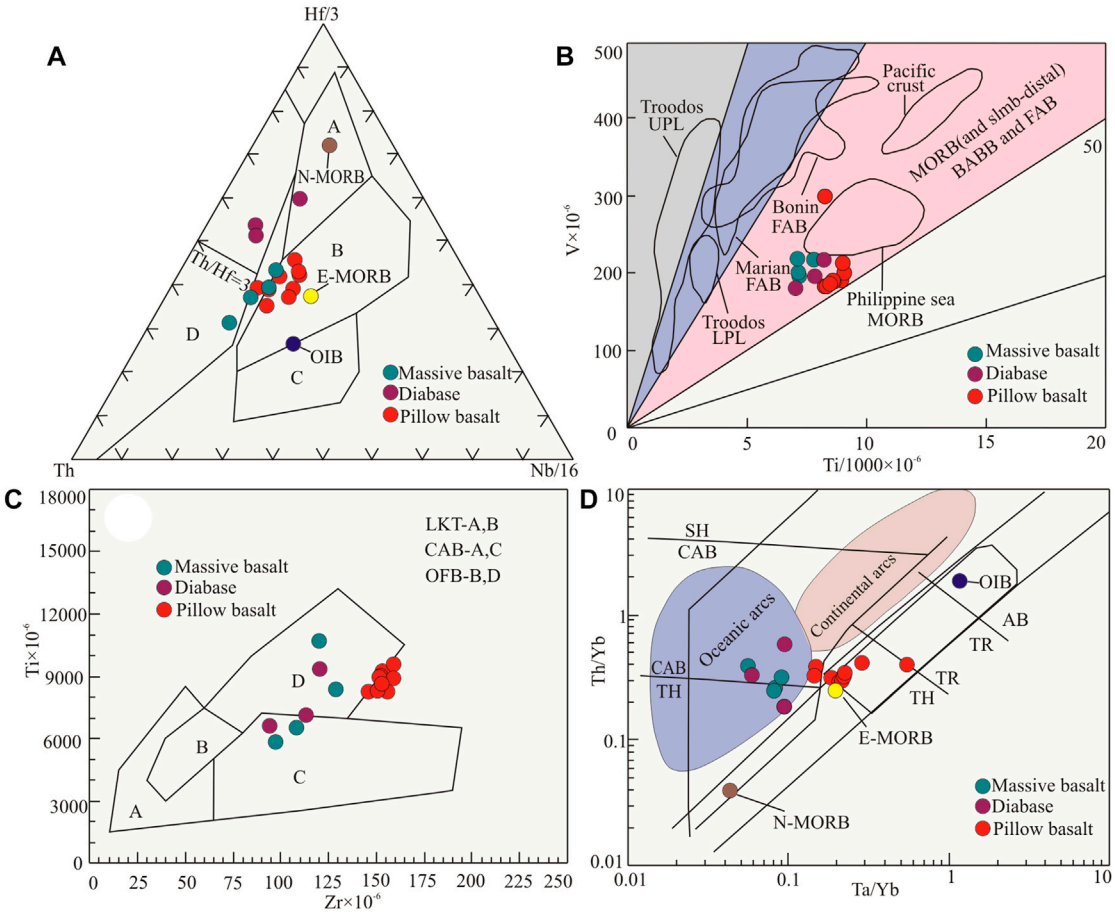

FIGURE 10
(A) Th-Hf-Nb diagram (Wood, 1980); **(B)** V-Ti diagram (Shervais, 1982); **(C)** Zr-Ti diagram (Pearce and Cann, 1973); and **(D)** Ta/Yb-Th/Yb diagram (Pearce, 1982) of the basic igneous rocks in the Bairin Right Banner area, Inner Mongolia. A, N-type MORB; B, E-type MORB and tholeiitic within-plate basalts and differentiates; C, Alkaline within-plate basalts and differentiates; D, Destructive plate-margin basalts and differentiates (Th/Hf>3 belong to Calc-alkaline basalt; Th/Hf<3 belong to tholeiitic basalt); BABB, back-arc basin basalt; FAB, fore-arc basalt; MORB, mid-ocean ridge basalt; LPL, lower pillow basalt; UPL, upper pillow basalt; LKT-A, B: low potassium tholeiite; CAB-A, C: calk-alkaline basalt; OFB-B, D: ocean floor basalt; AB: alkaline basalt; CAB: calk-alkaline basalt; SH: shoshonite; Th: tholeiitic basalt; TR: transitional basalt.

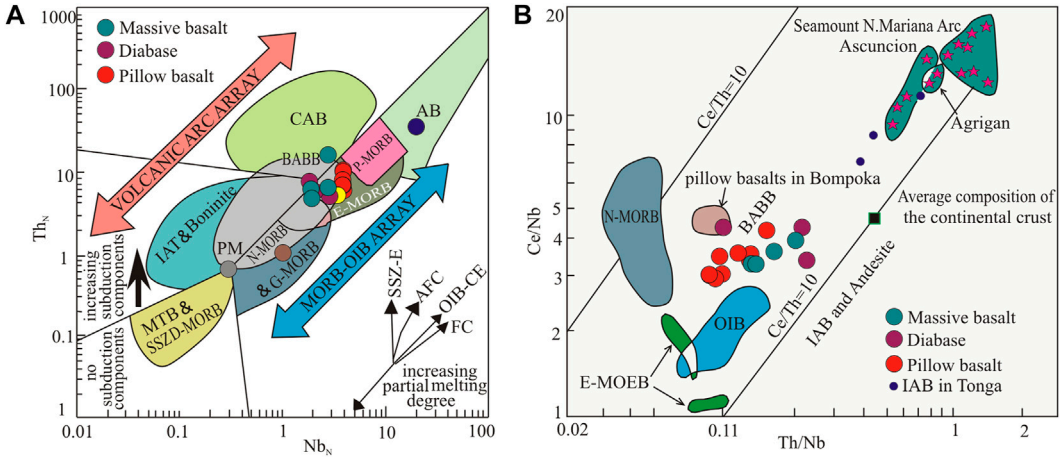

FIGURE 11
(A) Th_N-Nb_N diagram (Saccani, 2015); **(B)** Ce/Nb-Th/Nb diagram (Saunders and Tarney, 1991) of the basic igneous rocks in the Bairin Right Banner, Inner Mongolia. CAB, calk-alkaline basalt; AB, alkaline ocean-island basalt; N-MORB, normal mid-ocean ridge basalt; E-MORB, enriched mid-ocean ridge basalt; OIB, oceanic island basalt; IAT, island arc tholeiite; BABB, back-arc basin basalt; P-MORB, plume mid-ocean ridge basalt; G-MORB, garnet-influenced mid-ocean ridge basalt; MTB, medium-Ti basalt; SSZ, supra-subduction zone; SSZ-E, supra-subduction zone enrichment; AFC, assimilation-fractional crystallization; OIB-CE, ocean island-type (plume-type) component enrichment; FC, fractional crystallization.

In the primitive mantle-normalized incompatible element diagram (Figure 7), the distribution curves of massive basalt, diabase, and pillow basalt are similar, and the trace elements contents decrease with the decrease of element incompatibility, which are different from the "hump" type of the typical continental within-plate basalt and "big uplift" type of the oceanic island basalt. In general, the La/Ta ratios of island arc basalts and some depleted mid-ocean ridge basalts were greater than 15, and their Nb/La ratios were less than 1, while the La/Ta ratios of within-plate basalts and transitional mid-ocean ridge basalts were less than 15, and the Nb/La ratios were greater than 1 (Condie, 1989). The La/Ta values (32–51) and Nb/La values (0.59–0.84) of the massive basalts and diabases, respectively, were different from those of within-plate basalts and transitional mid-ocean ridge basalts. The element ratios of island arc basalts (Th/Yb > 0.1, Th/Nb > 0.07 and Hf/Th < 8) were opposite to those of the depleted mid-ocean ridge basalts (Condie, 1989). The Th/Yb values (0.19–0.56), Th/Nb values (0.10–0.23), and Hf/Th values (1.74–7.33) in both the massive basalts and diabases showed the characteristics of island arc basalt; similar findings can be observed in the Hf/3-Th-Nb/16, V-Ti, Ti-Zr, and Th/Yb-Ta/Yb diagrams, and they also show a certain affinity to enriched mid-ocean ridge basalt (Figure 7). The Nb contents of pillow basalt samples (8.4×10^{-6}–9.8×10^{-6}, average 9.2×10^{-6}) were similar to those of the enriched mid-ocean ridge basalts (8.3×10^{-6}), and Sr contents (259×10^{-6}–449×10^{-6}) were significantly higher than those of the enriched mid-ocean ridge basalts, which were in between those of E-MORB and ocean island basalt (OIB). Pillow basalts were relatively enriched in Ba and U, while slightly depleted in Rb and Th, which were similar to E-MORB, suggesting that they might have been formed in a similar setting. Although the trace elements composition and rare earth element (REE) distribution patterns of the pillow basalts were similar to E-MOBR, there were some differences, i.e., TiO_2 contents were similar to those of the back-arc basin basalts (Xu et al., 2003).

In the Th_N-Nb_N (Figure 11A) diagram, the massive basalt and diabase samples are plotted in the transition field between CAB and IAT, and close to the IAT field, while the pillow basalt samples fall in the E-MORB field, and the evolution trends of all the samples are consistent with those of the supra-subduction zone enrichment (SSZ-E). In the Th/Nb-Ce/Nb diagram (Figure 11B), the samples of massive basalts, diabases, and pillow basalts are plotted in the transition field of the pillow basalt in Bompoka and OIB.

To sum up, the formation of massive basalts and diabases was consistent with the arc magmatism of the Late Paleozoic in the region, which is extensively distributed in southeast Inner Mongolia. Pillow basalt showed geochemical affinity to E-MORB (Pearce, 2008; Furnes et al., 2012), such as pillow basalts in the Solund-Stavfjord ophiolite belt in Norway and pillow basalts in Bompoka, Andaman Islands, India (Furnes et al., 2012; Jafri and Sheikh, 2013). The composition of the basic igneous rocks in the Bairin Right Banner area had both the characteristics of MORB and island arc magmatic rocks, and rocks with such characteristics are usually produced above the subduction zone (Xu et al., 2003). The rare earth elements (REEs) and trace element characteristics of massive basalts, diabases, and pillow basalts were more similar to those of Okinawa Trough basalts (Shinjo et al., 1999). Therefore, we conclude that the massive basalt and diabase with island arc characteristics and the pillow basalt with E-MORB characteristics in the basic igneous rocks of Bairin Right Banner might have been formed by the subduction of oceanic crust in the depleted upper mantle and then reacted to mantle peridotite during the subduction of the Paleo-Asian Oceanic slab (Shinjo et al., 1999; Belousov et al., 2021).

5.4 Implications for tectonic evolution of the Paleo-Asian Ocean

From the initial subduction (~510 Ma) to the final closure, the Paleo-Asian Ocean experienced a complex tectonic evolution process (Xiao et al., 2003; Miao et al., 2007, 2008; Windley et al., 2007; Jian et al., 2010; Xu et al., 2014, 2015; Song et al., 2015; Zhang et al., 2016;

Dong et al., 2022). Ophiolites play an important role in studying the development and evolution history of ancient oceans. Solonker-Mandula ophiolite in the west of the Xar Moron suture zone was formed in a fore-arc setting as a result of intra-oceanic subduction during the Early Permian (290–284 Ma, Jian et al., 2010; Chen et al., 2012). In addition, the ophiolite in the Sonidyouqi area was formed in the mature back-arc basin during the Early Permian (297 Ma, Song et al., 2015). These ophiolites, in conjunction with the Paleozoic Island arc magmatic rocks on either side (Eizenhöfer et al., 2014; Song et al., 2015), indicate that the subduction of the Paleo-Asian Ocean in the west of the Xar Moron suture zone continued until the Early Permian (Jing et al., 2022).

During the Late Carboniferous to Early-Middle Permian, extensively magmatic events were witnessed in the Xilinhot to Bairin Right Banner area (Liu et al., 2022; Yang et al., 2022). The main rock types are calc-alkaline, high-potassium calc-alkaline, and alkaline rocks. These rock assemblages and their geochemical characteristics indicate that the rocks were formed in a subduction-induced island arc environment (Fan et al., 2012; Cheng et al., 2013; Zhang et al., 2018; Yang et al., 2022). In the Early Permian, rodingite (280 Ma) in the Xingshuwa ophiolite mélange was formed in the forearc-island arc environment (Song et al., 2015), and the Wudaoshimen pillow basalts (277 Ma) were formed in the normal mid-ocean ridge basalt (N-MORB) environment (Wang et al., 2014; Song et al., 2015). The formation of these rocks was related to the subduction of the Paleo-Asian Oceanic slab, suggesting that the Paleo-Asian Ocean was not closed in this period (Yang et al., 2022). The marine clastic-sedimentary rock series of the Shoushangou Formation, Dashizhai Formation, and Zhesi Formation were developed in the Middle-Lower Permian (Li, 2006); also, the development of Permian radiolarian fossils in chert of Xingshuwa ophiolite (Wang and Fan, 1997) indicate that the Paleo-Asian Ocean was still open in the Middle Permian. On the north bank of the Xar Moron River, the Upper Permian Linxi Formation changed from marine facies to continental facies, which is consistent with the sedimentary characteristics of a remnant ocean basin, rather than an extensional rift environment (Li, 2006; Zheng et al., 2014). The massive basalt (272.0 ± 2.8 Ma) and diabase (261.5 ± 3.2 Ma) in this study showed characteristics of oceanic island arc magmatic rocks, and the pillow basalt (256.5 ± 2.5 Ma) showed geochemical affinity to E-MORB, which indicates that there was still the remnant ocean basin of the Paleo-Asian Ocean in this period.

In the Late Permian, Angara flora and Cathaysian flora appeared on both sides of the Xar Moron River, such as the bivalves and bryozoan fossils in the Linxi Formation section in the Linxi area and the sporopollen fossils of the Xingfuzhilu Formation in the Bairin Right Banner area (Zhang et al., 2014; Shi et al., 2016). The study of paleomagnetic data of volcanic-sedimentary strata showed that the Songliao accretionary terrane and the northern margin of the North China Craton had reached around 30°N in the Permian (Ren et al., 2021; Jiang et al., 2022). In the Triassic, a large syn-collision or post-collision magmatic belt was formed as a result of the collision of the North China and the Siberian plates (Li et al., 2007; Wu et al., 2011; Eizenhöfer et al., 2014; Liu et al., 2014; Zhao et al., 2019; Zhao et al., 2021). A large magmatic belt was formed of Shuangjingzi Bimica granites (237–229 Ma), Zhuanshanzi granites (246 Ma), Jianshetun granites (249 Ma), Longtoushan granites (241–226 Ma), Xinlin granites (241 Ma), Lanjiayingzi granodiorites (242 Ma), Baiyinxile pasture monzonitic granites (246 Ma), Xilinhot granites (233 Ma), Yuanbaoshan granites (239 Ma), and Wuyingzi syenogranites (249 Ma) in the Keshiketengqi area. These granitic intrusions represent an intensive and important magmatic event in the Late Permian-Triassic (Liu et al., 2022).

The formation ages of massive basalt, diabase, and pillow basalt in the study area were from 272 Ma to 256 Ma, which were similar to those of the supra-subduction zone (SSZ) type ophiolite (Dilek and Furnes, 2011, 2014), and were the products of the subduction of the Paleo-Asian Oceanic slab in the Late Permian. Based on the regional geological data and previous studies, the remnant ocean basin of the Paleo-Asian Ocean might have been closed after the Late Permian. On this basis, we propose that the closure of the remnant ocean basin of the Paleo-Asian Ocean occurred after the Late Permian, not during the Late Devonian-Early Carboniferous, which indicates that the remnant ocean basin of the Paleo-Asian Ocean was finally closed along the Xar Moron suture zone.

6 Conclusion

1. The ages of massive basalt, diabase, and pillow basal in the Bairin Right Banner area are 272.0 ± 2.8 Ma, 261.5 ± 3.2 Ma, and 256.5 ± 2.5 Ma, respectively, indicating their formation during the Late Permian.
2. The massive basalts and diabases show the geochemical characteristics of subduction-derived island arc magmatic rocks, while the pillow basalts show geochemical affinity to E-MORB, which is similar to the SSZ type ophiolite. They were formed when the oceanic crust was subducted in the depleted upper mantle and reacted to mantle peridotite during the subduction of the Paleo-Asian Oceanic slab.
3. The basic igneous rocks in the Bairin Right Banner area are the embodiment of the subduction of the Paleo-Asian Oceanic slab in the Late Permian. Combined with the regional data and previous studies, the Paleo-Asian Ocean was finally closed along the Xar Moron suture zone during the Late Permian-Early Triassic, and the collision between the North China and Siberia plates might have occurred during the Early Triassic.

Data availability statement

The raw data supporting the conclusion of this article will be made available by the authors, without undue reservation. Requests to access the datasets should be directed to orcidme@163.com.

Author contributions

All authors were involved in the study. WY and CL initiated the idea and designed the studies. WY, AF, and BZ finished the field, petrology, and geochemical experiments. YY and BZ performed the zircon dating. XH and AF processed the geochemical data. WY and MA wrote the original manuscript.

Funding

This research is jointly funded by Heilongjiang Provincial Key R&D Program Project (No. GA21A204) and China Geological Survey Project (No. DD20160048-13).

Acknowledgments

We are highly indebted to the reviewers for their positive comments and suggestions. Thanks are extended to the colleagues in the State Key Laboratory of Geological Processes and Mineral Resources, China University of Geosciences, and Beijing Research Institute of Uranium Geology, for their valuable help to conduct LA-ICP-MS zircon U-Pb and trace element analyses.

Conflict of interest

The authors declare that the research was conducted in the absence of any commercial or financial relationships that could be construed as a potential conflict of interest.

Publisher's note

All claims expressed in this article are solely those of the authors and do not necessarily represent those of their affiliated organizations, or those of the publisher, the editors and the reviewers. Any product that may be evaluated in this article, or claim that may be made by its manufacturer, is not guaranteed or endorsed by the publisher.

Supplementary material

The Supplementary Material for this article can be found online at: https://www.frontiersin.org/articles/10.3389/ feart.2023.1109206/full#supplementary-material

References

Aldanmaz, E., Pearce, J. A., Thirlwall, M. F., and Mitchell, J. G. (2000). Petrogenetic evolution of late Cenozoic, post-collision volcanism in Western Anatolia, Turkey. *J. Volcanol. Geotheermal Res.* 102 (1-2), 67–95. doi:10.1016/s0377-0273(00)00182-7

Belousov, I., Batanova, V., Sobolev, A., Savelieva, G., Danyushevsky, L., and Draayers, E. (2021). Pyroxenites from mantle section of Voykar Ophiolite: Melt/peridotite reaction and crystallization in SSZ mantle. *Lithos* 388-389, 106063. doi:10.1016/j.lithos.2021.106063

Boynton, W. V. (1984). "Geochemistry of the rare Earth elements: Meteorite studies," in *Rare earth element geochemistry*. Editor P. Henderson (Amsterdam: Elsevier), 63–114.

Condie, K. C. (1989). Geochemical changes in basalts and andesites across the Archean-Proterozoic boundary: Identification and significance. *Lithos* 23 (1), 1–18.

Chen, C., Zhang, Z. C., Guo, Z. J., Li, J. F., Feng, Z. S., and Tang, W. H. (2012). Geochronology, geochemistry, and its geological significance of the Permian Mandula mafic rocks in Damaoqi, Inner Mongolia. *Sci. China Earth Sci.* 55, 39–52. doi:10.1007/s11430-011-4277-z

Cheng, T. S., Yang, W. J., and Wang, D. H. (2013). Zircon U-Pb age of the spilite-keratophyre sequence of the Dashizhai formation in the Maodeng of Xilinhaote, Inner Mongolia and its geological significance. *Geoscience* 27, 525–536.

Chu, H., Zhang, J. R., Wei, C. J., Wang, H. C., and Ren, Y. W. (2013). A new interpretation of the tectonic setting and age of meta-basic volcanics in the Ondor Sum Group, Inner Mongolia. *China Sci. Bull.* 58, 3580–3587. doi:10.1007/s11434-013-5862-7

Corfu, F., Hanchar, J. M., Hoskin, P. W., and Kinny, P. (2003). Atlas of zircon textures. *Rev. Mineral. Geochem* 53 (1), 469–500. doi:10.2113/0530469

Crawford, A. J., Falloon, T. J., and Eggins, S. (1987). The origin of island arc high-alumina basalts. *Contributions Mineralogy Petrology* 97 (3), 417–430. doi:10.1007/bf00372004

Dilek, Y., and Furnes, H. (2011). Ophiolite Genesis and global tectonics: Geochemical and tectonic fingerprinting of ancient oceanic lithosphere. *Geol. Soc. Am. Bull.* 123, 387–411. doi:10.1130/b30446.1

Dilek, Y., and Furnes, H. (2014). Ophiolites and their origins. *Elements* 10, 93–100. doi:10.2113/gselements.10.2.93

Dong, Y., Wang, S. M., Yu, Q., Chen, J. S., Yang, H., Ge, W. C., et al. (2022). Late Paleozoic tectonic-magmatic evolution history of the northeastern China. *Acta Petrol. Sin.* 38 (8), 2249–2268. doi:10.18654/1000-0569/2022.08.04

Eizenhöfer, P. R., Zhao, G. C., Zhang, J., and Sun, M. (2014). Final closure of the paleo-Asian ocean along the solonker suture zone: Constraints from geochronological and geochemical data of permian volcanic and sedimentary rocks. *Tectonics* 33, 441–463. doi:10.1002/2013tc003357

Fan, Z. L., Ke, Y. F., Chen, W., Yang, W. W., and Sun, X. F. (2012). Age and its tectonic significance of I-type granite in Xilinhot, inner Mongolia. *Resour. Survey& Environ.* 33 (3), 191–197.

Frey, F. A., Green, D. H., and Roy, S. D. (1978). Integrated models of basalt petrogenesis: A study of quartz tholeiites to olivine melilitites from South eastern Australia utilizing geochemical and experimental petrological data. *J. Petrology* 19 (3), 463–513. doi:10.1093/petrology/19.3.463

Furnes, H., Dilek, Y., and Pedersen, R. B. (2012). Structure,geochemistry,and tectonic evolution of trench-distal back arc oceanic crust in the Western Norwegian Caledonides,Solund-Stavfjord ophiolite (Norway). *Geol. Soc. Am. Bull.* 124 (7-8), 1027–1047. doi:10.1130/b30561.1

Hu, Z. C., Liu, Y. S., Chen, L., Zhou, L., Li, M., Zong, K. Q., et al. (2011). Contrasting matrix induced elemental fractionation in NIST SRM and rock glasses during laser ablation ICP-MS analysis at high spatial resolution. *J. Anal. Atomic Spectrom.* 26 (2), 425–430. doi:10.1039/c0ja00145g

Jafri, S. H., and Sheikh, J. M. (2013). Geochemistry of pillow basalts from Bompoka,Andaman-nicobar islands,Bay of bengal,India. *J. Asian Earth Sci.* 64, 27–37. doi:10.1016/j.jseaes.2012.11.035

Jian, P., Kröner, A., Windley, B. F., Shi, Y. R., Zhang, W., Zhang, L. Q., et al. (2012). Carboniferous and cretaceous mafic–ultramafic massifs in inner Mongolia (China): A shrimp zircon and geochemical study of the previously presumed integral "hegenshan ophiolite". *Lithos* 142-143, 48–66. doi:10.1016/j.lithos.2012.03.007

Jian, P., Liu, D. Y., Kroener, A., Windley, B. F., Shi, Y. R., Zhang, F. Q., et al. (2008). Time scale of an early to mid-Paleozoic orogenic cycle of the long-lived Central Asian Orogenic Belt,Inner Mongolia of China:Implications for continental growth. *Lithos* 101, 233–259. doi:10.1016/j.lithos.2007.07.005

Jian, P., Liu, D. Y., Kröner, A., Windley, B. F., Shi, Y. R., Zhang, W., et al. (2010). Evolution of a permian intraoceanic arc-trench system in the solonker suture zone,Central asian orogenic belt,China and Mongolia. *Lithos* 118, 169–190. doi:10.1016/j.lithos.2010.04.014

Jiang, Y., Jiang, S. H., Li, S. Z., Wang, G., Zhang, W., Lu, L. L., et al. (2022). Paleozoic to mesozoic micro-block tectonics in the eastern central asian orogenic belt:insights from magnetic and gravity anomalies. *Gondwana Res.* 102, 229–251. doi:10.1016/j.gr.2020.06.013

Jing, Y., Yang, H., Ge, W. C., Dong, Y., Ji, Z., Bi, J. H., et al. (2022). When did the final closure occur of the eastern Paleo-Asian Ocean:Constraints from the latest Early-Middle Triassic adakitic granites in the southeastern Central Asian Orogenic Belt. *Gondwana Res.* 103, 146–171. doi:10.1016/j.gr.2021.08.001

Li, C. D., Ran, H., Zhao, L. G., Wang, H. C., Zhang, K., Xu, Y. W., et al. (2012). LA-ICP-MS U-Pb geochronology of zircons from the Wenduermiao Group and its tectonic significance. *Acta Petrol. Sin.* 28 (11), 3705–3714.

Li, J. Y., Gao, L. M., Sun, G. H., Li, Y. P., and Wang, Y. B. (2007). Shuangjingzi middle Triassic syn-collisional crust-derived granite in the east Inner Mongolia and its constraint on the timing of collision between Siberian and Sino-Korean paleo-plates. *Acta Petrol. Sin.* 23 (3), 565–582.

Li, J. Y., Liu, J. F., Qu, J. F., Zheng, R. G., Zhao, S., Zhang, J., et al. (2019). Major geological features and crustal tectonic framework of Northeast China. *Acta Petrol. Sin.* 35 (10), 2989–3016. doi:10.18654/1000-0569/2019.10.04

Li, J. Y. (2006). Permian geodynamic setting of northeast China and adjacent regions: closure of the paleo-Asian Ocean and subduction of the paleo-pacific plate. *J. Asian EarthSciences* 26, 207–224. doi:10.1016/j.jseaes.2005.09.001

Li, X. H., Liu, Y., Tu, X. L., Hu, G. Q., and Zeng, W. (2002). Precise determination of chemical compositions in silicate rocks using ICP-AES and ICP-MS:A comparative study of sample digestion techniques of alkali fusion and acid dissolution. *Geochimica* 31 (3), 289–294.

Li, Y. L., Zhou, H. W., Brouwer, F. M., Wijbrans, J. R., Zhou, Z. Q., and Liu, H. F. (2011). Tectonic significance of the xilin gol complex, inner Mongolia, China: Petrological, geochemical and U–Pb zircon age constraints. *J. Asian Earth Sci.* 42, 1018–1029. doi:10.1016/j.jseaes.2010.09.009

Liu, J. F., Li, J. Y., Chi, X. G., Qu, J. F., Hu, Z. C., Fang, S., et al. (2013). A late-Carboniferous to early early-Permian subduction-accretion complex in Daqing pasture,southeastern Inner Mongolia:Evidence of northward subduction beneath the Siberian paleoplate southern margin. *Lithos* 177, 285–296. doi:10.1016/j.lithos.2013.07.008

Liu, J. F., Li, J. Y., Chi, X. G., Qu, J. F., Hu, Z. C., and Guo, C. L. (2014). Petrological and geochemical characteristics of the early triassic granite belt in southeastern inner Mongolia and its tectonic setting. *Acta Geol. Sin.* 88 (9), 1677–1690.

Liu, J. F., Li, J. Y., Sun, L. X., Yin, D. F., and Zheng, P. X. (2016). Zircon U-Pb dating of the Jiujingzi ophiolite in Bairin left Banner,Inner Mongolia:constraints on the formation and evolution of the xar Moron River suture zone. *Geol. China* 43 (6), 1947–1962.

Liu, J. F., Li, J. Y., Zhao, S., Zhang, J., Zheng, R. G., Zhang, W. L., et al. (2022). Crustal accretion and paleo-Asian ocean evolution during late paleozoic-early mesozoicin southeastern central asian orogenic belt:evidence from magmatism in linxi-dongwuqi area,southeastern inner Mongolia. *Acta Petrol. Sin.* 38 (8), 2181–2215. doi:10.18654/1000-0569/2022.08.02

Liu, Y. S., Gao, S., Hu, Z. C., Gao, C. G., Zong, K. Q., and Gao, D. B. (2010b). Continental and oceanic crust recycling-induced melt-peridotite interactions in the Trans-North China Orogen:U-Pb dating,Hf isotopes and trace elements in zircons from mantle xenoliths. *J. Petrology* 51 (1-2), 537–571. doi:10.1093/petrology/egp082

Liu, Y. S., Hu, Z. C., Zong, K. Q., Gao, C. G., Gao, S., Xu, J., et al. (2010a). Reappraisement and refinement of zircon U-Pb isotope and trace element analyses by LA-ICP-MS. *Chin. Sci. Bull.* 55 (15), 1535–1546. doi:10.1007/s11434-010-3052-4

Lu, L., Qin, Y., Zhang, K. J., Han, C. Y., Wei, T., Li, Z. F., et al. (2020). Provenance and tectonic settings of the late paleozoic sandstones in central inner Mongolia,NE China: constraints on the evolution of the southeastern central asian orogenic belt. *Gondwana Res.* 77, 111–135. doi:10.1016/j.gr.2019.07.006

Ludwig, K. R. (2003). *User's manual for isoplot 3.0:A geochronological toolkit for microsoft excel*. Berkeley: Berkeley Geochronology Center Special Publication, 1–71.

Luo, Z. W., Xu, B., Shi, G. Z., Zhao, P., Faure, M., and Chen, Y. (2016). Solonker ophiolite in Inner Mongolia, China:a late Permian continental margin-type ophiolite. *Lithos* 261, 72–91. doi:10.1016/j.lithos.2016.03.001

Miao, L. C., Fan, W. M., Liu, D. Y., Zhang, F. Q., Shi, Y. R., and Guo, F. (2008). Geochronology and geochemistry of the Hegenshan ophiolitic complex: Implications for late-stage tectonic evolution of the Inner Mongolia-Daxinganling Orogenic Belt,China. *J. Asian Earth Sci.* 32 (5), 348–370. doi:10.1016/j.jseaes.2007.11.005

Miao, L. C., Zhang, F., Fan, W. M., and Liu, D. Y. (2007). Phanerozoic evolution of the Inner Mongolia-Daxinganling orogenic belt in North China:constraints from geochronology of ophiolites and associated formations. *Geol. Soc.,Lond.,Spec. Publ.* 280 (1), 223–237. doi:10.1144/sp280.11

Miyashiro, A. (1974). Volcanic rock series in island arcs and active continental margins. *Am. J. Sci.* 274 (4), 321–355. doi:10.2475/ajs.274.4.321

Pang, Y. M., Guo, X. W., Zhang, X. H., Zhu, X. Q., Hou, F. H., Wen, Z. H., et al. (2020). Late mesozoic and cenozoic tectono-thermal history and geodynamic implications of the great xing'an range,NE China. *J. Asian Earth Sci.* 189, 104155. doi:10.1016/j.jseaes.2019.104155

Pearce, J. A., and Cann, J. R. (1973). Tectonic setting of basic volcanic rocks determined using trace element analyses. *Earth Planet. Sci. Lett.* 19 (2), 290–300. doi:10.1016/0012-821x(73)90129-5

Pearce, J. A. (2008). Geochemical fingerprinting of oceanic basalts with applications to ophiolite classification and the search for Archean oceanic crust. *Lithos* 100 (1), 14–48. doi:10.1016/j.lithos.2007.06.016

Pearce, J. A. (1982). "Trace element characteristics of lavas from destructive plate boundaries," in *Andesites*. Editor R. S. Thrope (New York: John Wiley & Sons), 528–548.

Polat, A., and Hofmann, A. W. (2003). Alteration and geochemical patterns in the 3.7-3.8 Ga Isua greenstone belt,west Greenland. *Precambrian Res.* 126 (3-4), 197–218. doi:10.1016/s0301-9268(03)00095-0

Ren, Q., Zhang, S. H., Sukhbaatar, T., Zhao, H. O., Wu, H. C., Yang, T. S., et al. (2021). Did the boreal realm extend into the equatorial region? New paleomagnetic evidence from the tuva-mongol and amuria blocks. *Earth Planet. Sci. Lett.* 576, 117246. doi:10.1016/j.epsl.2021.117246

Robinson, P. T., Zhou, M. F., Hu, X. F., Reynolds, P., Bai, W. J., and Yang, J. S. (1999). Geochemical constraintson the origin of the hegenshan Ophiolite,Inner Mongolia,China. *J. Asian Earth Sci.* 17 (4), 423–442. doi:10.1016/s1367-9120(99)00016-4

Rojas-Agramonte, Y., Kroner, A., Demoux, A., Xia, X., Wang, W., Donskaya, T., et al. (2011). Detrital and xenocrystic zircon ages from Neoproterozoic to Palaeozoic arc terranes of Mongolia:Significance for the origin of crustal fragments in the Central Asian Orogenic Belt. *Gondwana Res.* 19 (3), 751–763. doi:10.1016/j.gr.2010.10.004

Saccani, E. (2015). A new method of discriminating different types of post-Archean ophiolitic basalts and their tectonic significance using Th-Nb and Ce-Dy-Yb systematics. *Geosci. Front.* 6 (4), 481–501. doi:10.1016/j.gsf.2014.03.006

Saunders, A., and Tarney, J. (1991). *Back-arc basins floyda*. Oceanic Basalts, London: Blackie.

Sengör, A. M. C., Natal'In, B. A., and Burtman, V. S. (1993). Evolution of the Altaid tectonic collage and Palaeozoic crustal growth in Eurasia. *Nature* 364, 299–307. doi:10.1038/364299a0

Shervais, J. W. (1982). Ti-V plots and the petrogenesis of modern and ophiolitic lavas. *Earth Planet. Sci. Lett.* 59, 101–118. doi:10.1016/0012-821x(82)90120-0

Shi, G. Z., Song, G. Z., Wang, H., Huang, C. Y., Zhang, L. D., and Tang, J. R. (2016). Late Paleozoic tectonics of the Solonker Zone in the Wuliji area,InnerMongolia,China:Insights from stratigraphic sequence,chronology,and sandstone geochemistry. *Journalof Asian Earth Sci.* 127, 100–118. doi:10.1016/j.jseaes.2016.06.022

Shinjo, R., Chung, S. L., Kato, Y., and Kimura, M. (1999). Geochemical and Sr-Nd isotopic characteristics of volcanic rocks from the Okinawa Trough and Ryukyu Arc: Implications for the evolution of a young,intracontinental back arc basin. *J. Geophys. Res. Earth)* 104 (5), 10591–10608. doi:10.1029/1999jb900040

Song, S. G., Wang, M. M., Xu, X., Wang, C., Niu, Y. L., Allen, M. B., et al. (2015). Ophiolites in the Xing'an-Inner Mongolia accretionary belt of the CAOB: Implications for two cycles of seafloor spreading and accretionary orogenic events. *Tectonics* 34, 2221–2248. doi:10.1002/2015tc003948

Sun, S. S., and McDonough, W. F. (1989). Chemical and isotopic systematics of oceanic basalts:implications for mantle composition and processes. *Geol. Soc.,Lond.,Spec. Publ.* 42 (1), 313–345. doi:10.1144/gsl.sp.1989.042.01.19

Tang, J. Z., Zhang, Z. C., Xue, J. Z., Liu, B., Chen, Y., and Zhang, S. H. (2021). Permo-Carboniferous provenance shifts at the northern margin of the North China Craton and their tectonic implications:Detrital zircon U-Pb-Hf records from central Inner Mongolia. *Gondwana Res.* 95, 134–148. doi:10.1016/j.gr.2021.03.012

Tian, D. X., Yang, H., Ge, W. C., Zhang, Y. L., Chen, J. S., Chen, H. J., et al. (2018). Petrogenesis and tectonic implications of Late Carboniferous continental arc high-K granites in the Dongwuqi area,central Inner Mongolia,North China. *J. Asian Earth Sci.* 167, 82–102. doi:10.1016/j.jseaes.2018.07.010

Tong, Y., Jahn, B. M., Wang, T., Hong, D. W., Smith, E. I., Sun, M., et al. (2015). Permian alkaline granites in the Erenhot–Hegenshan belt, northern Inner Mongolia, China: Model of generation, time of emplacement and regional tectonic significance. *J. Asian Earth Sci.* 97, 320–336. doi:10.1016/j.jseaes.2014.10.011

Wang, Y. J., and Fan, Z. R. (1997). Discovery of Permian radiolarians in ophiolite belt on northern side of Xar moron river,Inner Mongolia and its geological significance. *Acta Palaeontol. Sin.* 36 (1), 58–69.

Winchester, J. A., and Floyd, P. A. (1977). Geochemical discrimination of different magma seriesand their differentiation products using immobile elements. *Chem. Geol.* 20, 325–343. doi:10.1016/0009-2541(77)90057-2

Windley, B. F., Alexeiev, D., Xiao, W. J., Kröner, A., and Badarch, G. (2007). Tectonic models for accretion of the central asian orogenic belt. *J. Geol. Soc.,Lond* 164, 31–47. doi:10.1144/0016-76492006-022

Wood, D. A. (1980). The application of a Th-Hf-Ta diagram to problems of tectonomagmatic classification and toestablishing the nature ofcrustal contamination of basaltic lavas of the British Tertiary volcanic province. *Earth Planet. Sci. Lett.* 20, 11–30. doi:10.1016/0012-821x(80)90116-8

Wu, F. Y., Sun, D. Y., Ge, W. C., Zhang, Y. B., Grant, M. L., Wilde, S. A., et al. (2011). Geochronology of the Phanerozoic granitoids in northeastern China. *J. Asian Earth Sci.* 41, 1–30. doi:10.1016/j.jseaes.2010.11.014

Wu, Y. B., and Zheng, Y. F. (2004). Genesis of zircon and its constraints on interpretation of U-Pb age. *Chin. Sci. Bull.* 49 (15), 1554–1569. doi:10.1360/04wd0130

Wang, Y. Y., Xu, B., Cheng, S. D., Liao, W., Shao, J., and Wang, Y. (2014). Zircon U-Pb dating of the mafic lava from Wudaoshimen, Hexigten, Inner Mongolia and its geological significance. *Acta Petrol. Sin.* 30 (7), 2055–2062.

Xiao, W. J., Windley, B. F., Hao, J., and Zhai, M. G. (2003). Accretion leading to collision and the Permian Solonker suture,Inner Mongolia,China:termination of the central Asian orogenic belt. *Tectonics* 22 (6), 1069. doi:10.1029/2002TC001484

Xiao, W. J., Windley, B. F., Huang, B. C., Han, C. M., Yuan, C., Chen, H. L., et al. (2009). End-Permian tomid-Triassic termination of the accretionary processes of the southern Altaids:implications for the geodynamic evolution,Phanerozoic continental growth,and metallogeny of Central Asia. *Int.J. Earth Sci.* 98, 1189–1217. doi:10.1007/s00531-008-0407-z

Xie, W., Luo, Z. Y., Xu, Y. G., Chen, Y. B., Hong, L. B., Ma, L., et al. (2016). Petrogenesis and geochemistry of the late Carboniferous rear-arc(or back-arc)pillow basaltic lava in the Bogda Mountains,Chinese North Tianshan. *Lithos* 244, 30–42. doi:10.1016/j.lithos.2015.11.024

Xu, B., Charvet, J., Chen, Y., Zhao, P., and Shi, G. Z. (2013). Middle Paleozoic convergent orogenic belts in Western Inner Mongolia(China):framework,kinematics,geochronology and implications for tectonic evolution of the Central Asian Orogenic Belt. *Gondwana Res.* 23, 1342–1364. doi:10.1016/j.gr.2012.05.015

Xu, B., Zhao, P., Bao, Q. Z., Zhou, Y. H., Wang, Y. Y., and Luo, Z. W. (2014). Preliminary study on thepre-Mesozoic tectonic unit division of the Xing-Meng Orogenic Belt (XMOB). *Acta Petrol. Sin.* 30 (7), 1841–1857.

Xu, B., Zhao, P., Wang, Y. Y., Liao, W., Luo, Z., Bao, Q., et al. (2015). The pre-Devonian tectonic framework of Xing'an-Mongolia orogenic belt (XMOB) in north China. *J. Asian Earth Sci.* 97, 183–196. doi:10.1016/j.jseaes.2014.07.020

Xu, G., Liu, H. C., Li, Y. L., Xu, Z., and Xie, Y. (2019). Early Permian Sunidyouqi supra subduction-zone ophiolites in the central Solonker suture zone (Inner Mongolia,China). *Geosci. Front.* 10, 1101–1111. doi:10.1016/j.gsf.2018.05.020

Xu, J. F., Castillo, P. R., Chen, F. R., Niu, H. C., Yu, X. Y., and Zhen, Z. P. (2003). Geochemistry of late Paleozoic mafic igneous rocks from the Kuerti area,Xinjiang.northwest China:implications for back-arc mantle evolution. *Chem. Geol.* 193 (1-2), 137–154. doi:10.1016/s0009-2541(02)00265-6

Yang, H., Ge, W. C., Ji, Z., Jing, J. H., Dong, Y., and Jing, Y. (2022). Phanerozoic magmatism and ocean continent framework of northeastern China and their relationship with climate change. *Acta Petrol. Sin.* 38 (5), 1443–1459. doi:10.18654/1000-0569/2022.05.11

Yang, J. F., Zhang, Z. C., Chen, Y., Yu, H. F., and Qian, X. Y. (2017). Ages and origin of felsic rocks from the eastern Erenhot ophiolitic complex,southeastern central asian orogenic Belt,Inner Mongolia China. *J. Asian Earth Sci.* 144, 126–140. doi:10.1016/j.jseaes.2016.12.049

Yang, S. H., Miao, L. C., Zhang, F. C., Zhu, M. S., Zhou, Y., Baatar, M. S., et al. (2019). Detrital zircon age spectra of the gurvan sayhan accretionary complex in South Mongolia: constraints on the late paleozoic evolution of the southern central asian orogenic belt. *J. Asian Earth Sci.* 175, 213–229. doi:10.1016/j.jseaes.2018.07.041

Yang, W. P., Zhang, S. X., Jiang, H. Y., Liu, H. D., Sui, C. Y., Sun, J. J., et al. (2018). Characteristics and geological implications of the late permian adakitic volcanic rocks from Bairin Right banner area,Inner Mongolia. *Geol. Bull. China* 37 (9), 1710–1721.

Yuan, H. L., Gao, S., Liu, X. M., Li, H. M., Günther, D., and Wu, F. Y. (2004). Accurate U-Pb age and trace element determinations of zircon by laser ablation inductively coupled plasmamass spectrometry. *Geostand. Geoanalytical Res.* 28 (3), 353–370. doi:10.1111/j.1751-908x.2004.tb00755.x

Zhang, J. R., Wei, C. J., Chu, H., and Chen, Y. P. (2016). Mesozoic metamorphismand its tectonic implication along the Solonker suture zone in central Inner Mongolia,China. *Lithos* 261, 262–277. doi:10.1016/j.lithos.2016.03.014

Zhang, S. H., Zhao, Y., Alfred, K., Liu, X. M., Xie, L. W., and Chen, F. K. (2009). Early Permian plutons from the northern North China Block:constraints on continental arc evolution and convergent margin magmatism related to the Central Asian Orogenic Belt. *Int. J. Earth Sci.* 98, 1441–1467. doi:10.1007/s00531-008-0368-2

Zhang, W., Jian, P., KrÖner, A., and Shi, Y. R. (2013). Magmatic and metamorphic development of an early to mid-Paleozoic continental margin arc in the southernmost Central Asian Orogenic Belt,Inner Mongolia,China. *J. Asian Earth Sci.* 72, 63–74. doi:10.1016/j.jseaes.2012.05.025

Zhang, X. F., Zhou, Y., Liu, J. L., Li, S. C., Wang, B. R., Teng, C., et al. (2018). Geochronology and geochemistry for volcanic rocks of Dashizhai Formation and its geological significance in Xi U jimqin Banner,Inner Mongolia. *Acta Petrol. Sin.* 34 (6), 1775–1791.

Zhang, Y. S., Tian, S. G., Li, Z. S., Gong, Y. X., Xing, E., Wang, Z. Z., et al. (2014). Discovery of marine fossils inthe upper part of the Permian Linxi Formation in Lopingian,Xingmeng area,China. *Chin. Sci. Bull.* 59 (1), 62–74. doi:10.1007/s11434-013-0036-1

Zhang, Z. C., Li, K., Li, J. F., Tang, W. H., Chen, Y., and Luo, Z. W. (2015). Geochronology and geochemistry of the eastern Erenhot ophiolitic complex: implications for the tectonic evolution of the inner Mongolia-daxinganling orogenic belt. *J. Asian Earth Sci.* 97, 279–293. doi:10.1016/j.jseaes.2014.06.008

Zhao, G. C., Cawood, P. A., Wilde, S. A., Sun, M., and Lu, L. (2000). Metamorphism of basement rocks in the Central Zone of the North China craton:implications for Paleoproterozoic tectonic evolution. *Precambrian Res.* 103, 55–88. doi:10.1016/s0301-9268(00)00076-0

Zhao, L., Li, Z. A., Li, J. Y., and Guo, F. (2019). Generation of Triassic post-collisional granitoids in the Linxi region(Inner Mongolia,NE China) and crustal growth in the eastern Central Asian.Orogenic Belt through melting of relict oceanic crust. *J. Asian Earth Sci.* 171, 348–362. doi:10.1016/j.jseaes.2018.08.032

Zhao, S., Liu, J. F., Zhang, Y. T., Zhang, J., Xu, W. L., and Li, J. Y. (2021). Geochronology and petrogenesis of the yuanbaoshan leucogranite in southeast Inner Mongolia: implications for the collision between the sino-Korean and siberian paleo-plates. *Lithos* 384-385, 105981. doi:10.1016/j.lithos.2021.105981

Zhao, X. C., Liu, C. Y., Wang, J. Q., Zhang, S. H., and Guan, Y. Z. (2020). Geochemistry,geochronology and Hf isotope of granitoids in the northern alxa region: implications for the late paleozoic tectonic evolution of the central asian orogenic belt. *Geosicence Front.* 11, 1711–1725. doi:10.1016/j.gsf.2020.01.009

Zheng, Y. J., Zhang, H. H., Chen, S. W., Zhang, J., Huang, X., Gong, F. H., et al. (2014). LA-ICP-MS U-Pb age of detrital zircons from late permian Linxi Formation in Ar horgin Banner,Inner Mongolia. *Geol. Bull. China* 33 (9), 1293–1307.

Zhou, J. B., Han, J., Zhao, G. C., Zhang, X. Z., Cao, J. L., Wang, B., et al. (2015). The emplacement time of the Hegenshan ophiolite:Constraints from the unconformably overlying Paleozoic strata. *Tectonophysics* 662, 398–415. doi:10.1016/j.tecto.2015.03.008

Zhou, J. B., Wilde, S. A., Zhang, X. Z., Zhao, G. C., Zheng, C. Q., Wang, Y. J., et al. (2009). The onset of Pacific margin accretion in NE China: Evidence from the Heilongjiang high-pressure metamorphic belt. *Tectonophysics* 478, 230–246. doi:10.1016/j.tecto.2009.08.009

Zhou, J. B., Wilde, S. A., Zhang, Z., and LiuLiu, F. L. J. H. (2012). Detrital zircons from phanerozoic rocks of the Songliao Block,NE China:Evidence and tectonic implications. *J. Asian Earth Sci.* 47, 21–34. doi:10.1016/j.jseaes.2011.05.004

Zhu, W. P., Tian, W., Wei, C. J., Shao, J. A., Fu, B., Fanning, C. M., et al. (2017). Late Paleozoic rift-related basalts from central Inner Mongolia,China. *J. Asian Earth Sci.* 144, 155–170. doi:10.1016/j.jseaes.2017.04.007